Icarus 429 (2025) 116401

Contents lists available at ScienceDirect

Icarus

journal homepage: www.elsevier.com/locate/icarus

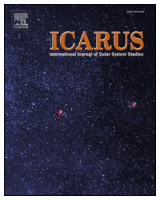

Inversion of ultraviolet occultation profiles in a dusty atmosphere: Analytic and numerical methods

B. Hubert [a,*], L. Soret [a], J.-C. Gérard [a], G. Wautelet [a], G. Munhoven [a], A. Piccialli [b], A.-C. Vandaele [b]

[a] Space sciences, Technologies and Astrophysics Research Institute, University of Liège, Liège, Belgium
[b] Royal Belgian Institute for Space Aeronomy, Brussels, Belgium

ARTICLE INFO

Keywords:
Mars
Atmosphere
Occultation
Inversion

ABSTRACT

Over the last two decades, important efforts have been undertaken by the most prominent space agencies to explore and analyze the interior, ground and atmosphere of Mars. A series of remote sensing instruments have been deployed and operated to characterize the atmospheric composition and dynamics. Several techniques have been used including solar occultation spectroscopy recording the sun spectrum attenuated through the atmosphere. We present three different methods dedicated to the analysis of occultation observations in the ultraviolet (UV) wavelength range covering the Hartley band of ozone. These methods are designed to account for several absorbing gases as well as aerosols responsible for extinction along the observing line-of-sight passing through the atmosphere. The aerosols are described using a local extinction parameter at a reference wavelength and a so-called Angström α-parameter to express the wavelength dependency of extinction with a power law.

In a first method, inverse Abel transform of the total extinction parameter (or optical thickness) of the atmosphere is conducted at each wavelength using a least-squares fitting technique, followed by a second least squares estimate of the local atmospheric properties at all fitting altitudes, separately.

A second method is derived in which all the atmospheric gas concentrations and aerosol extinction coefficient at reference wavelength vary with altitude in a piecewise linear manner. The α parameter is however assumed to be a piecewise linear function of ln(r), allowing for numerical and analytic developments. For the sake of inversion of the observation, the gas densities and aerosol reference extinction parameters are expressed as a function of the α parameters using a linear least-squares fitting expression, so that the α parameters can be estimated using a non-linear least-squares fitting method.

A third method is derived in which the gas species are approximated using piecewise exponential branches. Tests are conducted to evaluate the efficiency of all methods against retrieval of a prescribed atmospheric profile.

It is found that the first two methods can readily retrieve the atmospheric properties, the second one allowing for more consistent uncertainty estimates. The third method is found to be computationally expensive with a difficult-to-reach fitting convergence. Preliminary tests are conducted using TGO-NOMAD-UVIS observations in the O_3 Hartley band wavelength range. It is found that the CO_2 extinction is too weak to allow retrieval of the CO_2 density profile from observations at those wavelengths, while the O_3 density and dust properties can be successfully retrieved.

1. Introduction

Over the past decades, several space missions have been developed to explore the terrestrial planets of our solar system. The NASA Pioneer Venus [Colin and Hall, 1977; Colin and Hunten, 1977] mission is a key milestone in the exploration of Venus, later followed by the ESA Venus Express mission [Svedhem et al., 2007]. Mars has gained stronger attention owing to its resemblance to planet Earth, and to the expectation of finding out traces left by a water cycle and hopefully by ancient life forms. The ESA ExoMars mission [Vago et al., 2015] is part of an ambitious exploration project dedicated to the red planet, with other missions having recently been launched by other space agencies, such as

* Corresponding author.
E-mail address: B.Hubert@ulg.ac.be (B. Hubert).

https://doi.org/10.1016/j.icarus.2024.116401
Received 5 July 2024; Received in revised form 11 November 2024; Accepted 22 November 2024
Available online 26 November 2024

the NASA MAVEN [Jakosky et al., 2015] and ISRO MOM (Mangalayaan) [Kumar and Chauhan, 2014] missions. The U.A.E. SA EMM ("Hope") mission [Amiri et al., 2022] is another example of the successful international efforts made by the mankind to explore and understand our sister-planet.

The vast, comprehensive set of scientific projects towards Mars does not only focus on the planet's surface and subsurface geology. It also includes important efforts dedicated to the understanding of the planet atmosphere. In this context, the ExoMars mission included the Trace Gas Orbiter (TGO), carrying a suite of instruments specifically dedicated to the analysis of the atmosphere composition, photochemistry and dynamics. In particular, the Nadir and Occultation for MArs Discovery (NOMAD) [Neefs et al., 2015; Vandaele et al., 2015; Patel et al., 2017], developed and operated by the Belgian Institute for Space Aeronomy, is a three-channel spectrometer suite covering the electromagnetic spectrum from the infrared wavelength range (from 4.3 μm down to 2.2 μm) till the visible and ultraviolet domain (from 0.65 down to ~0.2 μm).

One of the several science targets of TGO-NOMAD is the measurement of the ozone (O_3) density profile in the ultraviolet (UV) 200–300 nm wavelength range, in which O_3 has been known for long to have a strong absorption band: the Hartley band system [Hartley, 1881]. Solar occultation profiles are regularly recorded by the instrument near the terminator, in order to allow for the retrieval of the gas density profile. The Mars atmosphere has carbon dioxide (CO_2) as vastly dominant specie. Although CO_2 is known to only weakly absorb light in the Hartley band UV range, its overwhelmingly large density leads to nevertheless consider and test it as a potential absorber, at least in some altitude ranges. Besides atmospheric gases, the Mars atmosphere is known to be variably loaded with aerosols, i.e. dusts, with extreme loading occurring during dust storms developing either locally (often in the "winter" hemisphere) or globally, then (non-uniformly) loading the whole atmosphere with dusts.

Dusts present in the atmosphere can produce extinction of sunlight, therefore often making a significant contribution to absorbance during solar occultation observations. Mattänen et al. [2013] examined occultation data from the Mars Express SPICAV instrument and analyzed the vertical distribution of the dust properties. They considered the (differential) extinction parameter of dusts (κ_0) at a reference wavelength of $\lambda_0 = 250$ nm and made the common assumption that the wavelength dependency of the extinction parameter varies as a power of wavelength λ [O'Neill and Royer, 1993; Angström, 1929], an assumption that previously prove reliable in the Earth's atmosphere over reasonably restricted wavelength ranges, the power being called the α or Angström parameter:

$$\kappa_\lambda = \kappa_0 \left(\frac{\lambda}{\lambda_0}\right)^{\alpha} \tag{1}$$

Extinction due to aerosols is then computed using a classical Beer-Lambert law, the optical thickness due to dusts, τ_λ^d, resulting from the line-of-sight integration of the extinction coefficient. If dust were the only cause of sun light extinction, this would read:

$$\begin{aligned} \tau_\lambda^d &= \int_{s_0}^{\infty} \kappa_\lambda(s)\, ds \\ I(\lambda) &= I_0(\lambda) exp\left(-\tau_\lambda^d\right) \end{aligned} \tag{2}$$

where $I_0(\lambda)$ is the unabsorbed intensity of the solar flux reaching the planet, and $I(\lambda)$ is the intensity of sun light reaching the observer staring at the sun through the atmosphere. Parameter s_0 in the integral of eq. (2) can be set to 0 when measuring the distance from the observer along the line-of-sight (l.o.s.). But this distance can also be conveniently measured from the point of the l.o.s. which is the closest to the planet center, i.e. from the so-called tangent point, as illustrated in Fig. 1. Parameter s_0 is

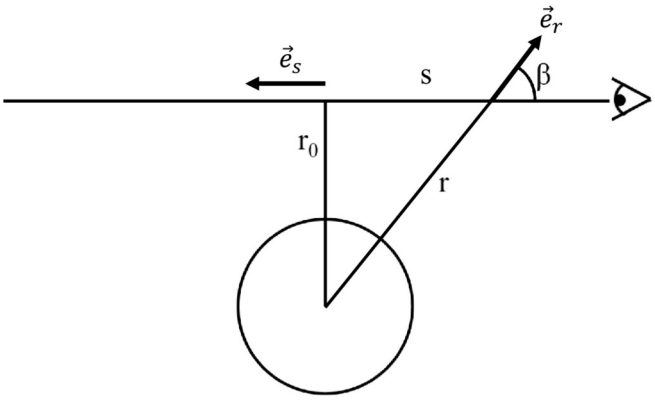

Fig. 1. Line-of-sight integration geometry. Variable s measures location along the line-of-sight (l.o.s.), from the tangent point located at distance r_0 from the planet center, where the radial direction is perpendicular to the l.o.s.. It is counted positively in the direction of a chosen reference unit vector $\vec{e}_s$. For a given value of r_0, angle β can also be used to specify the location along the l.o.s., and therefore the value of radial distance r and the orientation of the radial unit vector $\vec{e}_r$.

then a negative number, and tangent (planetocentric) altitude can be denoted r_0, the tangent altitude z_0 being defined by subtracting a reference planet radius from r_0. When the observer (i.e. an instrument onboard an orbiting satellite) is located far outside of the atmosphere, the l.o.s. integral can be carried out from -∞ to +∞ and s_0 is set to -∞.

When other absorbing gases, such as O_3 and CO_2 for example, need to be accounted for, the optical thickness at a given wavelength is the sum of the individual optical thicknesses of the different contributors to the absorption:

$$\begin{aligned} \tau_\lambda &= \tau_\lambda^d + \sum_{i=1}^{n_{sp}} \tau_\lambda^i \\ I(\lambda) &= I_0(\lambda)\, exp(-\tau_\lambda) \end{aligned} \tag{3}$$

where n_{sp} is the number of gas species to be accounted for, and τ_λ^i is the corresponding optical thickness obtained from the gas number density n_i and total extinction cross section (including absorption and scattering) $\sigma_i(\lambda)$:

$$\tau_\lambda^i = \int_{s_0}^{\infty} n_i(s)\, \sigma_i(\lambda)\, ds \tag{4}$$

Ideally, one should account for a possible dependency of the cross section with temperature, and therefore with radial distance r and l.o.s. distance s. In the temperature range prevailing in the atmosphere of Mars, this dependency can be expected to remain moderate [Malicet et al., 1995], and reasonable constant values will be adopted here, allowing to factor the cross section out of the integral for the sake of data analysis purposes, as will be discussed below.

A spherical symmetry assumption can often be safely made when computing l.o.s. integration of most quantities characterizing a planetary atmosphere. Indeed, the atmosphere of rocky planets can be regarded as a thin layer, with a radial extent much smaller than the planet radius, especially considering that the gas density and pressure mostly varies exponentially with altitude, so that significant contributions to the l.o.s. integral essentially come from a layer a few scale heights thick above the tangent point. Piccialli et al. [2021] showed, e.g., that even near the terminator, horizontal gradients only marginally influence solar light attenuation, along slant lines of sights, except at

high latitudes where it can make a ~ 20 % difference. Spherical assumption allows a simplification of the l.o.s. integrals of eqs. (2) and (4), reducing them to the so-called Abel transform of the integrant after the substitution $s = \sqrt{r^2 - r_0^2}$, $ds = \frac{r}{\sqrt{r^2-r_0^2}}\, dr$ separately for positive and negative values of s and assuming the observer is at sufficiently large altitude (so that integral over s can be considered from -∞ to + ∞). For any quantity f(r) for which a spherical symmetry assumption can be made, the l.o.s. integration of f(r), denoted $F(r_0)$, only depends on the tangent radius r_0 and can be written

$$F(r_0) = \int_{-\infty}^{\infty} f(s)\, ds = 2 \int_{r_0}^{\infty} \frac{r}{\sqrt{r^2 - r_0^2}}\, f(r)\, dr \tag{5}$$

where the second integral is the Abel transform of f(r). When spaceborne instruments provide measurement of $F(r_0)$ over a range of r_0 values and a spherical symmetry is assumed, retrieving f(r) requires evaluating the inverse Abel transform of $F(r_0)$ [Bracewell, 1999].

Many authors have described inverse Abel transform methods in many different contexts [e.g. Quémerais et al., 2006, Forget et al., 2009]. This study inherits a large part of its developments from Hubert et al. [2016] and [Hubert et al., 2022], and references therein. We only summarize here the essential ideas and results necessary for the current study. The reader is invited to consult those references for further details.

Analytic inverse Abel transform can be considered when $F(r_0)$ is known with an infinite accuracy:

$$f(r) = \frac{-1}{\pi} \int_r^{\infty} dr_0\, \frac{1}{\sqrt{r_0^2 - r^2}}\, \frac{dF(r_0)}{dr_0} \tag{6}$$

The integral of eq. (6) requires knowing the derivative of $F(r_0)$ over a large range of r_0 values. When $F(r_0)$ is provided by observation, accurately computing its derivative is problematic, since local variations can easily be dominated by the noise, which necessarily degrades the measured signal. Numerical inversion methods therefore need to be used, which mostly rely on least squares fitting techniques.

In order to produce a least-squares fitting method, one needs to discretize the problem and represent function f(r) using a sum of suitably chosen analytic basis functions. (Other non-linear representations may also be considered, though.) One can, for example, use a piecewise-linear representation of f(r) built as a sum of triangular functions defined over finite, bounded intervals:

$$\begin{aligned} t_k(r) &= \frac{r - r_{k-1}}{r_k - r_{k-1}} \chi_{[r_{k-1}, r_k[}(r) + \left(1 - \frac{r - r_k}{r_{k+1} - r_k}\right) \chi_{[r_k, r_{k+1}[}(r) \\ &= \frac{r - r_{k-1}}{r_k - r_{k-1}} \chi_{[r_{k-1}, r_k[}(r) + \frac{r_{k+1} - r}{r_{k+1} - r_k} \chi_{[r_k, r_{k+1}[}(r) \\ f(r) &= \sum_{k=1}^{n} a_k\, t_k(r) \end{aligned} \tag{7}$$

where function $\chi_{\Omega}(r)$ takes value 1 when $r \in \Omega$, 0 otherwise. Index k varies between 1 and n, and enumerates the set of triangles centered on radial distance r_k, parameters a_k are used to linearly combine the t_k terms and produce a piecewise linear representation of f(r). According to this series development, $f(r_k) = a_k$. The first (last) term of t_k is ignored when k = 1 (k = n, respectively). As the Abel transform is a linear operator, the Abel transform of f(r), $F(r_0)$ is obtained directly from the Abel transform of the $t_k(r)$, denoted $T_k(r_0)$:

$$\begin{aligned} T_k(r_0) &= \int_{r_0}^{\infty} \frac{r}{\sqrt{r^2 - r_0^2}}\, t_k(r)\, dr \\ F(r_0) &= \sum_{k=1}^{n} a_k\, T_k(r_0) \end{aligned} \tag{8}$$

The $T_k(r_0)$ are easily obtained defining the following set of indefinite integrals $I_n(r,r_0)$ and the recurrence that relates them [Hubert et al., 2016]:

$$\begin{aligned} I_n &= \int dr\, \frac{r}{\sqrt{r^2 - r_0^2}}\, r^n \\ (n+1) I_n &+ n\, r_0^2\, I_{n-2} = r^n \sqrt{r^2 - r_0^2} \\ I_{-1} &= arcosh\left(\frac{r}{r_0}\right) = ln\left(\frac{r}{r_0} + \sqrt{\frac{r^2}{r_0^2} - 1}\right) \\ I_0 &= \sqrt{r^2 - r_0^2} \end{aligned} \tag{9}$$

In the particular case of the triangular elements of Eq. (8), only the $n = 0$ and $n = 1$ cases will be used, but there is no formal restriction to the computation of indefinite integrals involving higher degree polynomials if necessary. Each I_n is defined up to an additive constant that we can take to be 0 as we are only interested in using them for the computation of definite integrals. When observation provides $F(r_0)$ at a set of tangent radius values $r_{0,j}$, retrieving f(r) expressed as a piecewise-linear function amounts to estimating the a_k using a least squares-fit method, as explained, e.g., in Hubert et al. [2016, 2022]. This least-squares fit inversion however relies on the solution of a linear system, which is often somewhat ill-conditioned. This problem is generally overcome using Tikhonov regularization, i.e. by adding to the classical least-squares fit matrix another matrix. This matrix is used to evaluate a quantity related to f(r), such as the square of its second derivative for example, that we expect should remain relatively small. Indeed, noisy variations of f(r) would produce artificial, unrealistic, large values of its derivatives. Moreover, adding such a regularization matrix produces a new matrix whose diagonal elements are different. For a symmetric matrix, this modifies the set of eigenvalues and generally tends to produce a matrix that has a determinant sufficiently different from 0 to cure the ill-conditioning of the original system. This is obtained, though, at the expense of a modification of the concept of optimum: the fitted function is not only expected to represent the data, but also to keep its second derivative (or another property) as small as possible.

Several authors have already applied inverse Abel transform techniques to both solar and stellar occultation measurements to study the atmosphere of Mars. Quémerais et al. [2006] proposed an inversion method based on a regularized onion peeling technique to study stellar occultations in the far ultraviolet (FUV) spectral range and estimate the CO_2 density profile, as well as Forget et al. [2009]. Montmessin et al. [2006] rather focused on aerosols. Määttänen et al. [2013] also used an inversion technique to characterize the aerosol climatology. Piccialli et al. [2023] compared three inversion techniques applied to retrieve the ozone density profile of Mars, in the presence of aerosols, including a sophisticated method based on radiative transfer modelling aimed at accounting for horizontal gradients near the terminator in the case of solar occultation. Piccialli et al. [2021] evaluated that horizontal gradients generally play a minor role in solar occultation inversions, excepted at high latitude where they can make a 20 % difference over the estimated ozone density. Määttänen et al. [2022] conducted an

analysis of solar and stellar occultation of the Mars atmosphere to characterize the ozone profile and distribution. The studies listed above mostly relied on observations acquired by the ESA ExoMars and Mars Express missions. Stellar occultation studies were also conducted using observations from the NASA MAVEN mission by, e.g., Gupta et al. [2022] who studied the density and temperature profile of the planet. In the present study, we detail three inversion techniques dedicated to the analysis of occultation observations of atmospheres containing aerosols and absorbing gases. The methods we propose share several characteristics with the method of Quémerais et al. [2006], while taking advantage of new, original analytic developments.

2. Analytic developments

The basic concept of Inverse Abel transform developed in the introduction needs to be modified, in order to analyze occultation observations of a planetary atmosphere, especially when aerosols need to be included, in which case, as it will be explained below, the wavelength dependency of extinction also needs being assessed. In the case of occultation, the observed quantity is the exponential of $-\tau_\lambda(r_0)$, i.e. an exponential of some line-of-sight integration of the absorbers properties, instead of only the line-of-sight integration of the local emission rate when studying an (unabsorbed) airglow layer. A logarithm has therefore to be computed at some stage before inverting the Abel transform. Moreover, observation is obtained at different wavelengths and, in the case of the aerosols, the α-parameter can depend on altitude. This will unavoidably result in a non-linear problem. We will first introduce analytic results that can be obtained when making suitably chosen assumptions over the altitude dependency of the dusts properties. Then we will propose several methods to actually implement the least-squares based inverse-Abel transform allowing to retrieve the absorbing gas density and dust property profiles.

2.1. Analytic representation of the dusts optical thickness

The local (differential) extinction parameter for dust at reference wavelength λ_0, κ_0, can be represented using the piecewise-linear expression given by eq. (7). It could be tempting to use the same kind of piecewise-linear expression for the altitude-dependent α parameter. But another functional dependency can instead be assumed, considering that this parameter appears as a power of the wavelength ratio in eq. (1). A linear dependency with respect to r would unavoidably introduce exponential functions in the Abel transform expression. Although it is possible to find stably converging analytic series development for such integrals [Hubert et al., 2022], these results are not easy to manipulate. In contrast, building the triangles of eq. (7) using ln(r) instead of r makes it possible to commute the formal roles of wavelength and radial distance. Introducing a reference radius r* in order to have dimensionless quantities as argument of the logarithm function, we define triangular functions $u_k(r)$ as

$$u_k(r) = \frac{ln\left(\frac{r}{r^*}\right) - ln\left(\frac{r_{k-1}}{r^*}\right)}{ln\left(\frac{r_k}{r^*}\right) - ln\left(\frac{r_{k-1}}{r^*}\right)}\chi_{]r_{k-1},r_k[}(r) + \frac{ln\left(\frac{r_{k+1}}{r^*}\right) - ln\left(\frac{r}{r^*}\right)}{ln\left(\frac{r_{k+1}}{r^*}\right) - ln\left(\frac{r_k}{r^*}\right)}\chi_{]r_k,r_{k+1}[}(r)$$
$$= \frac{ln\left(\frac{r}{r_{k-1}}\right)}{ln\left(\frac{r_k}{r_{k-1}}\right)}\chi_{]r_{k-1},r_k[}(r) + \frac{ln\left(\frac{r}{r_{k+1}}\right)}{ln\left(\frac{r_k}{r_{k+1}}\right)}\chi_{]r_k,r_{k+1}[}(r) \quad (10)$$

$$\alpha(r) = \sum_{k=1}^{n} \alpha_k\, u_k(r)$$

With these expressions, $\alpha(r)$ varies piecewise-linearly with ln(r). Given that $\chi_\Omega(r)$ is 0 for any r outside of interval Ω, one can then express the (differential) extinction coefficient of the aerosols as

$$\kappa_k(r,\lambda) = \kappa_{0,k}\, t_k(r) \left(\frac{\lambda_0}{\lambda}\right)^{\alpha(r)}$$
$$= \kappa_{0,k}\left[\frac{r - r_{k-1}}{r_k - r_{k-1}}\chi_{]r_{k-1},r_k[}(r) \left(\frac{\lambda_0}{\lambda}\right)^{\alpha_{k-1}\, u_{k-1}(r)+\alpha_k u_k(r)+\alpha_{k+1}u_{k+1}(r)} + \right.$$
$$\left.\frac{r_{k+1} - r}{r_{k+1} - r_k}\chi_{]r_k,r_{k+1}[}(r)\left(\frac{\lambda_0}{\lambda}\right)^{\alpha_{k-1}u_{k-1}(r)+\alpha_k\, u_k(r)+\alpha_{k+1}u_{k+1}(r)}\right]$$
$$= \kappa_{0,k}\left[\frac{r - r_{k-1}}{r_k - r_{k-1}}\chi_{]r_{k-1},r_k[}(r) \left(\frac{\lambda_0}{\lambda}\right)^{\alpha_{k-1}\, u_{k-1}(r)+\alpha_k u_k(r)} + \right.$$
$$\left.\frac{r_{k+1} - r}{r_{j+1} - r_k}\chi_{]r_k,r_{k+1}[}(r)\left(\frac{\lambda_0}{\lambda}\right)^{\alpha_k\, u_k(r)+a_{k+1}u_{k+1}(r)}\right]$$
$$= \kappa_{0,k}\left[\frac{r - r_{k-1}}{r_k - r_{k-1}}\chi_{]r_{k-1},r_k[}(r) \left(\frac{\lambda_0}{\lambda}\right)^{\alpha_{k-1}\frac{ln\left(\frac{r_k}{r^*}\right)-ln\left(\frac{r}{r^*}\right)}{ln\left(\frac{r_k}{r^*}\right)-ln\left(\frac{r_{k-1}}{r^*}\right)}+\alpha_k\frac{ln\left(\frac{r}{r^*}\right)-ln\left(\frac{r_{k-1}}{r^*}\right)}{ln\left(\frac{r_k}{r^*}\right)-ln\left(\frac{r_{k-1}}{r^*}\right)}} + \right.$$
$$\left.\frac{r_{k+1} - r}{r_{k+1} - r_k}\chi_{]r_k,r_{k+1}[}(r)\left(\frac{\lambda_0}{\lambda}\right)^{\alpha_k\frac{ln\left(\frac{r_{k+1}}{r^*}\right)-ln\left(\frac{r}{r^*}\right)}{ln\left(\frac{r_{k+1}}{r^*}\right)-ln\left(\frac{r_k}{r^*}\right)}+\alpha_{k+1}\frac{ln\left(\frac{r}{r^*}\right)-ln\left(\frac{r_k}{r^*}\right)}{ln\left(\frac{r_{k+1}}{r^*}\right)-ln\left(\frac{r_k}{r^*}\right)}}\right] \quad (11)$$

Note that the k[th] triangular element of the extinction coefficient is evaluated between r_{k-1} and r_{k+1}. Between r_{k-1} and r_k, the Angström parameter is given by a linear combination of the triangular elements u_{k-1} and u_k while between r_k and r_{k+1}, it is given by a linear combination of triangular elements u_k and u_{k+1}. As a consequence, there is a formal coupling between neighboring bins through the Angström parameter, making appear the α_{k-1} and α_{k+1} in the expression of κ_k. Now, the power of the wavelength ratio can be transformed into a power of the radial distance, which, as we will see, allows for particular expressions and formula in the Abel transform integral. For example,

$$\left(\frac{\lambda_0}{\lambda}\right)^{\alpha_k\frac{ln\left(\frac{r_{k+1}}{r^*}\right)-ln\left(\frac{r}{r^*}\right)}{ln\left(\frac{r_{k+1}}{r^*}\right)-ln\left(\frac{r_k}{r^*}\right)}+\alpha_{k+1}\frac{ln\left(\frac{r}{r^*}\right)-ln\left(\frac{r_k}{r^*}\right)}{ln\left(\frac{r_{k+1}}{r^*}\right)-ln\left(\frac{r_k}{r^*}\right)}} =$$
$$= exp\left(ln\left(\frac{\lambda_0}{\lambda}\right)\left(\alpha_k\frac{ln\left(\frac{r_{k+1}}{r^*}\right)-ln\left(\frac{r}{r^*}\right)}{ln\left(\frac{r_{k+1}}{r^*}\right)-ln\left(\frac{r_k}{r^*}\right)}+\alpha_{k+1}\frac{ln\left(\frac{r}{r^*}\right)-ln\left(\frac{r_k}{r^*}\right)}{ln\left(\frac{r_{k+1}}{r^*}\right)-ln\left(\frac{r_k}{r^*}\right)}\right)\right)$$
$$= \left(\frac{r}{r^*}\right)^{ln\left(\frac{\lambda_0}{\lambda}\right)\frac{\alpha_{k+1}-\alpha_k}{ln\left(\frac{r_{k+1}}{r^*}\right)-ln\left(\frac{r_k}{r^*}\right)}}\left(\frac{\lambda_0}{\lambda}\right)^{-\frac{\alpha_{k+1}ln\left(\frac{r_k}{r^*}\right)-\alpha_k\, ln\left(\frac{r_{k+1}}{r^*}\right)}{ln\left(\frac{r_{k+1}}{r^*}\right)-ln\left(\frac{r_k}{r^*}\right)}} \quad (12)$$

so that the radial dependency, which previously appeared in an exponent of the wavelength, now reduces to a power of r, more suitable for use in Abel transform integrals. The wavelength-dependent optical thickness of the dusts along a line-of-sight of tangent radius r_0, $\tau^d_\lambda(r_0)$ can now be expressed as follows:

$$\tau_\lambda^d(r_0) = 2\int_{r_0}^{\infty} \frac{r}{\sqrt{r^2-r_0^2}}\,\kappa_\lambda(r)\,dr$$
$$= 2\sum_{k=1}^{n}\int_{r_0}^{\infty} \frac{r}{\sqrt{r^2-r_0^2}}\,\kappa_k(r,\lambda)\,dr$$
$$= 2\sum_{k=1}^{n}\int_{r_0}^{\infty}\kappa_{0,k}\left[\frac{r-r_{k-1}}{r_k-r_{k-1}}\chi_{]r_{k-1},r_k[}(r)\left(\frac{r}{r^*}\right)^{\frac{\ln\left(\frac{\lambda_0}{\lambda}\right)(\alpha_k-\alpha_{k-1})}{\ln\left(\frac{r_k}{r^*}\right)-\ln\left(\frac{r_{k-1}}{r^*}\right)}}\left(\frac{\lambda_0}{\lambda}\right)^{-\frac{\alpha_k\ln\left(\frac{r_{k-1}}{r^*}\right)-\alpha_{j-1}\ln\left(\frac{r_k}{r^*}\right)}{\ln\left(\frac{r_k}{r^*}\right)-\ln\left(\frac{r_{k-1}}{r^*}\right)}}\right.$$
$$\left.+\frac{r_{k+1}-r}{r_{k+1}-r_k}\chi_{]r_k,r_{k+1}[}(r)\left(\frac{r}{r^*}\right)^{\frac{\ln\left(\frac{\lambda_0}{\lambda}\right)(\alpha_{k+1}-\alpha_k)}{\ln\left(\frac{r_{k+1}}{r^*}\right)-\ln\left(\frac{r_k}{r^*}\right)}}\left(\frac{\lambda_0}{\lambda}\right)^{-\frac{\alpha_{k+1}\ln\left(\frac{r_k}{r^*}\right)-\alpha_k\ln\left(\frac{r_{k+1}}{r^*}\right)}{\ln\left(\frac{r_{k+1}}{r^*}\right)-\ln\left(\frac{r_k}{r^*}\right)}}\right]\frac{r}{\sqrt{r^2-r_0^2}}\,dr \tag{13}$$

If we now denote $R_k = \max(r_k, r_0)$ and use the properties of the characteristic function $\chi_\Omega(x)$, we can write the dust optical thickness as

$$\tau_\lambda^d(r_0) = 2\sum_{k=1}^{n}\kappa_{0,k}\left[\left(\frac{\lambda_0}{\lambda}\right)^{-\frac{\alpha_k\ln\left(\frac{r_{k-1}}{r^*}\right)-\alpha_{k-1}\ln\left(\frac{r_k}{r^*}\right)}{\ln\left(\frac{r_k}{r^*}\right)-\ln\left(\frac{r_{k-1}}{r^*}\right)}}\right.$$
$$\int_{R_{k-1}}^{R_k}\frac{r}{\sqrt{r^2-r_0^2}}\frac{r-r_{k-1}}{r_k-r_{k-1}}\left(\frac{r}{r^*}\right)^{\frac{\ln\left(\frac{\lambda_0}{\lambda}\right)(\alpha_k-\alpha_{k-1})}{\ln\left(\frac{r_k}{r^*}\right)-\ln\left(\frac{r_{k-1}}{r^*}\right)}}dr \tag{14}$$
$$+\left(\frac{\lambda_0}{\lambda}\right)^{-\frac{\alpha_{k+1}\ln\left(\frac{r_k}{r^*}\right)-\alpha_k\ln\left(\frac{r_{k+1}}{r^*}\right)}{\ln\left(\frac{r_{k+1}}{r^*}\right)-\ln\left(\frac{r_k}{r^*}\right)}}$$
$$\left.\int_{R_k}^{R_{k+1}}\frac{r}{\sqrt{r^2-r_0^2}}\frac{r_{k+1}-r}{r_{k+1}-r_k}\left(\frac{r}{r^*}\right)^{\frac{\ln\left(\frac{\lambda_0}{\lambda}\right)(\alpha_{k+1}-\alpha_k)}{\ln\left(\frac{r_{k+1}}{r^*}\right)-\ln\left(\frac{r_k}{r^*}\right)}}dr\right]$$

All integrals appearing in Eq. (14) can be reduced to a difference of two integrals of the form

$$J_p = \int_{r_0}^{R}\frac{r}{\sqrt{r^2-r_0^2}}\,r^m\left(\frac{r}{r^*}\right)^p dr \tag{15}$$

with m being either 1 or 0. We now transform the integral of Equation (15) applying several consecutive substitutions: $x = r/r_0$ with Jacobian $1/r_0$ ($dx = dr/r_0$), then $y = \sqrt{x^2-1}$, $x = \sqrt{y^2+1}$ with Jacobian $\frac{y}{\sqrt{y^2+1}}$ so that

$$J_p = r_0\int_{r_0}^{R}\frac{r/r_0}{\sqrt{\left(\frac{r}{r_0}\right)^2-1}}\,r_0^m\left(\frac{r}{r_0}\right)^m\left(\frac{r_0}{r^*}\frac{r}{r_0}\right)^p dr\Big/ r_0$$
$$= \left(\frac{r_0}{r^*}\right)^p r_0^{m+1}\int_1^{\frac{R}{r_0}}\frac{x}{\sqrt{x^2-1}}x^{p+m}dx \tag{16}$$

and finally,

$$J_p = \left(\frac{r_0}{r^*}\right)^p r_0^{m+1}\int_0^{\sqrt{\left(\frac{R}{r_0}\right)^2-1}}\left(y^2+1\right)^{\frac{p+m}{2}}dy \tag{17}$$

We can now further transform the result of Eq. (17) to make appear Euler's integral representation of Gauss's hypergeometric ${}_2F_1$ function, which is usually defined from a series development [Abramowitz and Stegun, 1972, Olver et al., 2010]

$${}_2F_1(a,b,c,z) = \sum_{i=1}^{\infty}\frac{(a)_i\,(b)_i}{(c)_i}\frac{z^i}{i!}$$
$${}_2F_1(a,b,c,z) = \frac{\Gamma(c)}{\Gamma(b)\Gamma(c-b)}\int_0^1 t^{b-1}(1-t)^{c-b-1}(1-z\,t)^{-a}dt \tag{18}$$

where $\Gamma(x)$ is the usual gamma function, and $(a)_i$ denotes the Pochhammer symbol defined as $(a)_i = 1$ when $i = 0$ and $(a)_i = a\,(a+1)\ldots(a+i-1)$ when $i > 0$. We use two substitutions successively applied from Eq. (17): $y = \sqrt{\left(\frac{R}{r_0}\right)^2-1}\,v$, $dy = \sqrt{\left(\frac{R}{r_0}\right)^2-1}\,dv$, followed by $t = v^2$, $dv = \frac{1}{2\sqrt{t}}dt$:

$$J_p = \left(\frac{r_0}{r^*}\right)^p r_0^{m+1}\int_0^1\sqrt{\left(\frac{R}{r_0}\right)^2-1}\left(\left(\left(\frac{R}{r_0}\right)^2-1\right)v^2+1\right)^{\frac{p+m}{2}}dv$$
$$= \frac{1}{2}\left(\frac{r_0}{r^*}\right)^p r_0^{m+1}\sqrt{\left(\frac{R}{r_0}\right)^2-1}\int_0^1 t^{-\frac{1}{2}}\left(\left(\left(\frac{R}{r_0}\right)^2-1\right)t+1\right)^{\frac{p+m}{2}}dt \tag{19}$$

We can now directly apply the integral representation of ${}_2F_1$ given in

Eq. (18) by letting a = −(p + m)/2, b = 1/2, c = 3/2 (so that c-b-1 = 0) and $z = 1 - \left(\frac{R}{r_0}\right)^2$, which is negative. Given that $\Gamma(1/2) = \sqrt{\pi}$, $\Gamma(1) = 1$ and $\Gamma(3/2) = \sqrt{\pi}/2$, this leads to

$$J_p = \left(\frac{r_0}{r^*}\right)^p r_0^{m+1} \sqrt{\left(\frac{R}{r_0}\right)^2 - 1}\ {}_2F_1\left(-\frac{p+m}{2}, \frac{1}{2}, \frac{3}{2}, 1 - \left(\frac{R}{r_0}\right)^2\right) \tag{20}$$

an elegant result that opens possibilities to use properties and identities characterizing the hypergeometric function, especially considering that, for practical applications, $1 - \left(\frac{R}{r_0}\right)^2$ will be close to 0, or at least will have a module smaller than 1, the convergence radius of the defining series development of function ${}_2F_1$, avoiding the complications of analytic continuation. We anticipate here over the following paragraphs to emphasize that we expect that those identities and properties could be used to solve the problem of inverse Abel transform fitting and retrieval of the non-linear α parameter, but that it could not be efficiently done mostly because those identities lead to expressions making appear differences of the α parameter values at different altitudes (explicitly, differences of the α_j), so that iterative non-linear resolution methods lead to values determined up to an additive constant, which could hardly be retrieved.

The ranges of altitudes and α parameter values that can be expected to be relevant for the study of dusts lead to series developments (from Eq. (18)) that can hardly be summed up accurately. Identities between hypergeometric functions can however be used to cure that problem, but we found that directly relying on the integral expressions is finally more efficient from a numerical and computational standpoint. Indeed, the integral of Eq. (17) appears quite well suited for an integration using a Gauss-Legendre method (see, e.g. Press et al., 1992). This method is known to accurately integrate polynomials. A n-nodes Gauss-Legendre method does exactly compute integrals of any polynomial of degree 2n-1 or less. The integrant in Eq. (17) is a non-integer power producing a smooth, non-singular function, so that it can be expected to be efficiently integrated using a Gauss-Legendre method as well, especially over restricted integration intervals. Indeed, the sequence of substitutions leading to that expression got rid of the Jacobian of the Abel transform, which becomes singular near the tangent point, i.e. in the altitude range producing the largest contribution to the line-of-sight integration.

The above developments therefore bear two interesting results. First, they offer an analytic expression suitable for further analytic developments (if special functions such as ${}_2F_1$ can be considered analytic expressions as an exponential or a logarithm would). Second, they highlight an intermediate result which is particularly suited for numerical treatments. We also emphasize that computing the integral transforms of Eq. (14) using differences of hypergeometric functions can lead to a loss of numerical accuracy when the quantities to be subtracted from each other are nearly equal. If they differ after, say, their fourth significant digit, the loss of significant digits using 64-bit real number representation reduces the accuracy to some 12 significant digits instead of 16. When dealing with ill-conditioned problems such as inversions, it is safer avoiding such loss.

We can now write the wavelength-dependent optical thickness of dusts, represented over an altitude grid using the triangular elements defined in Eq. (13) and defining $\mathscr{J}^d$ as

$$\begin{aligned}\mathscr{J}^d(p,m,r_0,R) &= \int_{r_0}^{R} \frac{r}{\sqrt{r^2 - r_0^2}}\, r^m \left(\frac{r}{r^*}\right)^p dr \\ &= r_0^{m+1} \left(\frac{r_0}{r^*}\right)^p \left[z\ {}_2F_1\left(-\frac{m+p}{2}, \frac{1}{2}, \frac{3}{2}, -z^2\right)\right]_{z=\sqrt{\left(\frac{R}{r_0}\right)^2 - 1}}\end{aligned} \tag{21}$$

so that

$$\begin{aligned}\tau_\lambda^d(r_0) = {} & 2\sum_{k=1}^{n} \frac{\kappa_{0,k}}{r_k - r_{k-1}} \left(\frac{\lambda_0}{\lambda}\right)^{-\frac{\alpha_k \ln\left(\frac{r_{k-1}}{r^*}\right) - \alpha_{k-1} \ln\left(\frac{r_k}{r^*}\right)}{\ln\left(\frac{r_k}{r^*}\right) - \ln\left(\frac{r_{k-1}}{r^*}\right)}} \\ & \Big[\mathscr{J}^d(p,1,r_0,R_k) - \mathscr{J}^d(p,1,r_0,R_{k-1}) \\ & - r_{k-1}\left(\mathscr{J}^d(p,0,r_0,R_k) - \mathscr{J}^d(p,0,r_0,R_{k-1})\right)\Big]_{p=\ln\left(\frac{\lambda_0}{\lambda}\right)\frac{\alpha_k - \alpha_{k-1}}{\ln\left(\frac{r_k}{r^*}\right) - \ln\left(\frac{r_{k-1}}{r^*}\right)}} \\ & + 2\sum_{k=1}^{n} \frac{\kappa_{0,k}}{r_{k+1} - r_k} \left(\frac{\lambda_0}{\lambda}\right)^{-\frac{\alpha_{k+1} \ln\left(\frac{r_k}{r^*}\right) - \alpha_k \ln\left(\frac{r_{k+1}}{r^*}\right)}{\ln\left(\frac{r_{k+1}}{r^*}\right) - \ln\left(\frac{r_k}{r^*}\right)}} \\ & \Big[\mathscr{J}^d(p,1,r_0,R_{k+1}) - \mathscr{J}^d(p,1,r_0,R_k) \\ & + r_{k+1}\left(\mathscr{J}^d(p,0,r_0,R_{k+1}) - \mathscr{J}^d(p,0,r_0,R_k)\right)\Big]_{p=\ln\left(\frac{\lambda_0}{\lambda}\right)\frac{\alpha_{k+1} - \alpha_k}{\ln\left(\frac{r_{k+1}}{r^*}\right) - \ln\left(\frac{r_k}{r^*}\right)}}\end{aligned} \tag{22}$$

Quite obviously, the differences between $\mathscr{J}^d$ functions that appear in Eq. (22) can be expressed as integrals over a restricted domain, i.e. between two nodes of the grid of r_k values (with again $R_k = \max(r_0, r_k)$):

$$\begin{aligned}\mathscr{J}^d(p,1,r_0,R_k) - \mathscr{J}^d(p,1,r_0,R_{k-1}) &= \int_{R_{k-1}}^{R_k} \frac{r}{\sqrt{r^2 - r_0^2}}\, r \left(\frac{r}{r^*}\right)^p dr \\ \mathscr{J}^d(p,0,r_0,R_k) - \mathscr{J}^d(p,0,r_0,R_{k-1}) &= \int_{R_{k-1}}^{R_k} \frac{r}{\sqrt{r^2 - r_0^2}} \left(\frac{r}{r^*}\right)^p dr \\ \mathscr{J}^d(p,1,r_0,R_{k+1}) - \mathscr{J}^d(p,1,r_0,R_k) &= \int_{R_k}^{R_{k+1}} \frac{r}{\sqrt{r^2 - r_0^2}}\, r \left(\frac{r}{r^*}\right)^p dr \\ \mathscr{J}^d(p,0,r_0,R_{k+1}) - \mathscr{J}^d(p,0,r_0,R_k) &= \int_{R_k}^{R_{k+1}} \frac{r}{\sqrt{r^2 - r_0^2}} \left(\frac{r}{r^*}\right)^p dr\end{aligned} \tag{23}$$

These integrals can be transformed using the substitutions used to obtain Eq. (17) to produce expressions more suitable for numerical integration with a Gauss-Legendre method:

$$\begin{aligned}\mathscr{J}^d(p,1,r_0,R_k) - \mathscr{J}^d(p,1,r_0,R_{k-1}) &= \left(\frac{r_0}{r^*}\right)^p r_0^2 \int_{\sqrt{\left(\frac{R_{k-1}}{r_0}\right)^2 - 1}}^{\sqrt{\left(\frac{R_k}{r_0}\right)^2 - 1}} (y^2+1)^{\frac{p+1}{2}}\, dy \\ \mathscr{J}^d(p,0,r_0,R_k) - \mathscr{J}^d(p,0,r_0,R_{k-1}) &= \left(\frac{r_0}{r^*}\right)^p r_0 \int_{\sqrt{\left(\frac{R_{k-1}}{r_0}\right)^2 - 1}}^{\sqrt{\left(\frac{R_k}{r_0}\right)^2 - 1}} (y^2+1)^{\frac{p}{2}}\, dy \\ \mathscr{J}^d(p,1,r_0,R_{k+1}) - \mathscr{J}^d(p,1,r_0,R_k) &= \left(\frac{r_0}{r^*}\right)^p r_0^2 \int_{\sqrt{\left(\frac{R_k}{r_0}\right)^2 - 1}}^{\sqrt{\left(\frac{R_{k+1}}{r_0}\right)^2 - 1}} (y^2+1)^{\frac{p+1}{2}}\, dy \\ \mathscr{J}^d(p,0,r_0,R_{k+1}) - \mathscr{J}^d(p,0,r_0,R_k) &= \left(\frac{r_0}{r^*}\right)^p r_0 \int_{\sqrt{\left(\frac{R_k}{r_0}\right)^2 - 1}}^{\sqrt{\left(\frac{R_{k+1}}{r_0}\right)^2 - 1}} (y^2+1)^{\frac{p}{2}}\, dy\end{aligned} \tag{24}$$

For the sake of inversion using least squares fitting technique, the derivative of $\tau_\lambda^d(r_0)$ with respect to all relevant parameters, i.e. with respect to the $\kappa_{0,j}$ and α_j are needed. Derivative with respect to $\kappa_{0,j}$ is straightforward. The α_j appear in the expression of parameter p in the

above integrals, so that the chain rule needs to be applied, and derivative with respect to parameter p can be commuted within the integration. Applying the same sequence of variable substitutions as those used to derive Eq. (17), we finally obtain

$$\begin{aligned}&\frac{\partial}{\partial p}\left(\mathscr{I}^d(p,m,r_0,R_2)-\mathscr{I}^d(p,m,r_0,R_1)\right)=\\&ln\left(\frac{r_0}{r^*}\right)\left(\mathscr{I}^d(p,m,r_0,R_2)-\mathscr{I}^d(p,m,r_0,R_1)\right)\\&+\left(\frac{r_0}{r^*}\right)^p r_0^{m+1}\int_{\sqrt{\left(\frac{R_1}{r_0}\right)^2-1}}^{\sqrt{\left(\frac{R_2}{r_0}\right)^2-1}}\left(y^2+1\right)^{\frac{p+m}{2}}ln\left(\sqrt{y^2+1}\right)\,dy\end{aligned} \tag{25}$$

where R_1 and R_2 stand for any of the upper and lower integration bounds (respectively) appearing in Eq. (23). Evaluating all other derivatives needed to compute the derivatives of $\tau_\lambda^d(r_0)$ is straightforward, though lengthy and tedious. The integrant in the new integral of Eq. (25) only differs from the other integrals by a multiplication by a logarithm. This integrant remains smooth and can again be integrated numerically using the Gauss-Legendre method.

The developments carried up to now allow us to express the dust vertical profile using a sum of triangular elements including a complex wavelength dependence. They also allow evaluating its Abel transform to express the dusts optical thickness, as well as its derivative with respect to all the parameters appearing in the triangular elements. After Eqs. (11) to (13), we define the dust triangular elements over a discretized radial grid r_k, $t_k^d(\lambda,r)$, as well as its Abel transform $T_k^d(\lambda,r_0)$ as follows:

$$\begin{aligned}t_k^d(\lambda,r)&=t_k(r)\left(\frac{\lambda_0}{\lambda}\right)^{\alpha_{k-1}\ u_{k-1}(r)+\alpha_k u_k(r)}\\&=\frac{r-r_{k-1}}{r_k-r_{k-1}}\chi_{]r_{k-1},r_k[}(r)\left(\frac{r}{r^*}\right)^{\frac{ln\left(\frac{\lambda_0}{\lambda}\right)(\alpha_k-\alpha_{k-1})}{ln\left(\frac{r_k}{r^*}\right)-ln\left(\frac{r_{k-1}}{r^*}\right)}}\left(\frac{\lambda_0}{\lambda}\right)^{-\frac{\alpha_k ln\left(\frac{r_{k-1}}{r^*}\right)-\alpha_{k-1}\,ln\left(\frac{r_k}{r^*}\right)}{ln\left(\frac{r_k}{r^*}\right)-ln\left(\frac{r_{k-1}}{r^*}\right)}}\\&+\frac{r_{k+1}-r}{r_{k+1}-r_k}\chi_{]r_k,r_{k+1}[}(r)\left(\frac{r}{r^*}\right)^{\frac{ln\left(\frac{\lambda_0}{\lambda}\right)(\alpha_{k+1}-\alpha_k)}{ln\left(\frac{r_{k+1}}{r^*}\right)-ln\left(\frac{r_k}{r^*}\right)}}\left(\frac{\lambda_0}{\lambda}\right)^{-\frac{\alpha_{k+1}ln\left(\frac{r_k}{r^*}\right)-\alpha_k\,ln\left(\frac{r_{k+1}}{r^*}\right)}{ln\left(\frac{r_{k+1}}{r^*}\right)-ln\left(\frac{r_k}{r^*}\right)}}\\T_k^d(\lambda,r_0)&=2\int_{r_0}^{\infty}\frac{r}{\sqrt{r^2-r_0^2}}t_k^d(\lambda,r)\end{aligned} \tag{26}$$

and the dusts optical thickness is obtained along a slant line of sight with tangent radius r_0:

$$\tau_\lambda^d(r_0)=\sum_{k=1}^{n_d}\kappa_{0,k}\ T_k^d(\lambda,r_0) \tag{27}$$

We can also write the wavelength-dependent optical thickness of the ambient gas species as well. Let $[g_i]$ denote the number density of the i^{th} gas species, which we represent here using piecewise linear profiles build using a linear combination of triangle functions, and $\sigma_i(\lambda)$ its wavelength-dependent extinction cross section, assumed to be negligibly dependent on temperature and therefore on altitude:

$$\begin{aligned}[g_i](r)&=\sum_{k=1}^{n_g}a_k^i t_k(r)\\\tau_\lambda^i(r_0)&=\sum_{k=1}^{n_g}a_k^i\,\sigma_i(\lambda)\ T_k(r_0)\end{aligned} \tag{28}$$

where n_g is the number of altitude nodes used to discretize the gas density profile, which does not necessarily need to be equal to the number of nodes used to build the piecewise representation of the dusts profile. Indeed, each specie and dusts may be described over different discretization grids, although it is not mandatory.

The total extinction optical thickness along a slant line-of-sight with tangent radius r_0 is then the sum of the contributions from all absorbers, as given by Eq. (3)

$$\tau_\lambda(r_0)=\sum_{i=1}^{n_{sp}}\sum_{k=1}^{n_g}a_k^i\,\sigma_i(\lambda)\ T_k(r_0)+\sum_{k=1}^{n_d}\kappa_{0,k}\ T_k^d(\lambda,r_0) \tag{29}$$

Parameters a_j^i and $\kappa_{0,j}$ explicitly appear in a linear manner, while the non-linear dependency with respect to the α_j is hidden in the expression of $T_j^d(\lambda,r_0)$, after Eq. (26).

In practice, observation will provide measurements of the (attenuated) sun intensity over a set of lines-of-sights, i.e. for a set of r_0 values, $r_{0,i}$, and at a given set of wavelengths λ_l, $l=1,\ldots,L$. Considering that the unattenuated intensity, $I_{top,l}$, is known at all observing wavelengths from the observation at the largest tangent radius, the observed intensity $I_{j,l}$ can be divided by $I_{top,l}$ and the logarithm of this ratio can be computed, so that for each observing tangent radius and wavelength, the observation-derived optical thickness $\tau_{\lambda_l}^{obs}(r_{0,j})$ is given by

$$\tau_{\lambda_l}^{obs}(r_{0,j})=-ln\left(\frac{I_{j,l}}{I_{top,l}}\right) \tag{30}$$

The total optical thickness is therefore known in a manner that does not depend on the absolute calibration of the instrument used to acquire the data, nor on the units used to express them (as expected, since the optical thickness is a unit-less quantity). In principle the intensity ratio should be a positive number. When dealing with real data, very low intensities can artificially produce negative numbers after background subtraction, owing to noise contamination. When such a situation arises, the observed intensity may be replaced by a small positive number, especially if 0 is in the 2-σ interval bracketing the intensity (σ stands here for the standard deviation characterizing the noise affecting the observation). Indeed, in that case the negative value does not significantly differ from 0. When an intensity is found to be significantly negative considering the relevant uncertainty of the measurement, it can safely be considered that something went wrong, and this negative measurement should be ignored. Negative intensities should anyway have a small weight in any least squares fitting treatment, as it will be developed below. It can also be considered that those negative intensities will arise in the bottom side of observed occultation profiles, where only a few photons can be expected to be detected. This low intensity then prevents from obtaining meaningful physical parameters in that altitude range owing to the large uncertainties affecting the data, and one may even prefer ignoring the very bottom side of the observed profile, where the observed intensity is too low for accurate parameters determination: when there is no significant signal, there is not much that can be done.

2.2. Straightforward, two-steps inversion

One could consider that the optical thickness of Eq. (30) results from the line-of-sight integration of a differential optical thickness $\delta\tau_{\lambda l}(r)$ to be related to the relevant fitting parameters, i.e. the a_k^i, $\kappa_{0,k}$ and α_k. In a first step, the $\delta\tau_{\lambda l}(r)$ is then represented as a piecewise linear function produced as a linear combination of triangles t_k as defined in Eq. (7), using a grid of radial distances r_k and linear coefficients $\theta_{k,l}$:

$$\begin{aligned}\delta\tau_{\lambda l}(r) &= \sum_{k=1}^{n} \theta_{k,l}\, t_k(r) \\ \tau_{\lambda l}(r_0) &= 2\int_{r_0}^{\infty} \frac{r}{\sqrt{r^2 - r_0^2}}\, \delta\tau_{\lambda l}(r) \\ &= \sum_{k=1}^{n} \theta_{k,l}\, T_k(r_0)\end{aligned} \tag{31}$$

so that $\tau_{\lambda_l}(r_{0,j})$ is expressed as the Abel transform of $\delta\tau_{\lambda l}(r)$. Determining $\delta\tau_{\lambda l}(r_k)$ then reduces to fitting parameters $\theta_{k,l}$, which can be achieved quite directly using an inverse Abel transform fitting applied to the $\tau^{obs}_{\lambda_l}(r_{0,j})$ (which we can simply re-write $\tau^{obs}_{l,j}$) including regularization, such as described in Hubert et al. [2016], for example. The inversion provides the parameters $\theta_{k,l}$ as well as an estimate of their standard deviation.

The second step is, at each altitude, to determine all the relevant, local parameters using a least-squares fitting again, i.e. for any given k, estimating the a^i_k, $\kappa_{0,k}$ and α_k using the wavelength dependence of the differential optical thickness. We will then have

$$\theta_{k,l} = \sum_{i=1}^{n_{sp}} a^i_k \sigma_i(\lambda_l) + \kappa_{0,k} \left(\frac{\lambda_0}{\lambda_l}\right)^{\alpha_k} \tag{32}$$

For any given value of α_k and knowing $\theta_{k,l}$ over a set of discrete wavelength values λ_l, parameters a^i_k and $\kappa_{0,k}$ appear linearly in Eq. (32), so that they can be determined in a straightforward manner using a (weighted) linear least squares fitting for any prescribed α_k. It is then easy deriving a dichotomic search method (or any more sophisticated non-linear resolution method) that finds the best α_k value. Giving a weight w^k_l to each wavelength bin based on the standard deviation of $\theta_{k,l}$, we can use standard fitting techniques to reduce the right-hand-side of Eq. (32) to a function of parameter α_k only, and express the other, linear parameters as functions of α_k. In this context, for each prescribed α_k, retrieving the other parameters at the k^{th} fitting altitude then amounts to solving a least squares fit problem reducing to a linear system of equations, which is conveniently expressed in matrix format as follows. Let us define $\vec{\theta}_k = \left(\theta_{k,1}\sqrt{w^k_1}, \ldots, \theta_{k,L}\sqrt{w^k_L}\right)^+$ and $\vec{q}_k = \left(a^1_k, \ldots, a^{n_{sp}}_k, \kappa_{0,k}\right)$. The matrixes U_k and H_k of the minimization linear system are defined after equating the derivatives of the usual χ^2_k function with respect to the linear parameters to zero, and the expression of the system second member vector, $\vec{b}_k$, naturally follows:

$$\chi^2_k = \sum_{l=1}^{L} \left(\sum_{i=1}^{n_{sp}} a^i_k \sigma_i(\lambda_l) + \kappa_{0,k} \left(\frac{\lambda_0}{\lambda_l}\right)^{\alpha_k} - \theta_{k,l} \right)^2 w^k_l$$

$$U_k = \begin{pmatrix} \sigma_1(\lambda_1)\sqrt{w^k_1} & \cdots & \sigma_1(\lambda_L)\sqrt{w^k_L} \\ \vdots & & \vdots \\ \sigma_{n_{sp}}(\lambda_1)\sqrt{w^k_1} & \cdots & \sigma_{n_{sp}}(\lambda_L)\sqrt{w^k_L} \\ \left(\frac{\lambda_0}{\lambda_1}\right)^{\alpha_k}\sqrt{w^k_1} & \cdots & \left(\frac{\lambda_0}{\lambda_L}\right)^{\alpha_k}\sqrt{w^k_L} \end{pmatrix}^+ ; \quad \vec{b}_k = U^+_k \vec{\theta}_k \tag{33}$$

$$H_k = U_k\, U^+_k \qquad H_k \vec{q}_k = \vec{b}_k$$

Solving the last system of Eq. (33) provides the linear parameters as a function of the non-linear parameter α_k, allowing the search for an optimal α_k value minimizing the χ^2_k. It is also possible obtaining the uncertainties on the fitting parameters, either using standard formulas or using a bootstrapping method. Under standard assumptions, the variance-covariance matrix of the set of fitting parameters determined using least squares fit can be estimated from the inverse of the Hessian matrix of the χ^2 function, estimated near its minimum [Press et al., 1992]. In the present case with only one fitting parameter (the α_k), the Hessian matrix reduces to the second derivative of the χ^2 function. Once the variance over the α_k is known, those of the linear parameters can be estimated using usual error propagation formulas.

The straightforward method developed above may be used for obtaining a first guess for all the fitting parameters of the full inversion problem. Indeed, it does not fully account for possible covariance between the parameters, especially across different altitudes. A method that comprehensively fits the parameters at all altitudes and wavelengths at once is expected to be less prone to such issue. It is generally understood that all the parameters of a least squares fitting problem should be determined simultaneously as their optimal values are not necessarily independent on each other, especially when noise introduces uncertainties in the problem.

It can be noticed here that, although the knowledge of the unattenuated intensity (or brightness) may seem critical, it is not really the case. The analytic inverse Abel transform of Eq. (6) relies on the derivative of the Abel transform function with respect to the tangent radius. Therefore, the inverse Abel transform is not sensitive to any constant offset. And indeed, if we write I_{top} the observed topside intensity and I_∞ the actual unattenuated intensity, we successively obtain:

$$\begin{aligned}\tau(r_0) &= -ln\left(\frac{I(r_0)}{I_\infty}\right) \\ &= -ln\left(\frac{I(r_0)}{I_{top}}\frac{I_{top}}{I_\infty}\right) \\ &= -ln\left(\frac{I(r_0)}{I_{top}}\right) - ln\left(\frac{I_{top}}{I_\infty}\right)\end{aligned} \tag{34}$$

so that the inverse Abel transform of the observed $\tau(r_0)$ does not depend on a misattributed topside intensity. This conclusion must however not be overplayed: practical inverse Abel transform methods are based on least squares fitting techniques applied to a discrete set of observations gathered across a bounded interval of tangent altitudes. This situation differs from the analytic treatment, so that one cannot exclude some influence of a slightly inaccurate topside intensity, but this influence should not be expected to be dramatic either, besides the complexity incurred by a possible ill-conditioning, which holds for any kind of inaccuracy.

2.3. Coupled linear-nonlinear method

The complete inverse Abel transform fitting problem can also be expressed combining all altitudes and wavelengths in a consistent manner. As a part of the parameters appear in a non-linear manner in the functions that must be fitted (i.e. the α_k appear as exponent of the wavelength), the whole problem can be considered non-linear. A first approach can then be considered: treating the whole fitting problem as non-linear and using a general non-linear least-squares fitting algorithm, such as the Levenberg-Marquardt method [Press et al., 1992], to estimate all the fitting parameters. On the other hand, one can follow a reasoning comparable to what was proposed in Section 2.2 and consider that all the linear parameters have a definite value determined using a linear least-squares fitting method, as soon as the value of all the non-linear parameters (i.e. the α_k) are fixed. The linear parameters then appear as functions of the α_k, and the non-linear least squares fitting method only needs being applied to the non-linear parameters, i.e. the α_k.

As it is often the case with inversion problems, the inverse Abel transform fitting can be ill-conditioned. Technically, this means that the result of the inversion is over-sensitive to any disturbance, due to the matrix of the problem (especially concerning the linear parameters) having a small determinant or, in a more general mathematical context, because the problem eigenvalues range over many orders of magnitude. Under those conditions, at least one of them can be considered null when

compared with the largest one, from a numerical standpoint. Consequently, a regularization technique needs to be used [Press et al., 1992], which transforms the original problem into another one that has nearly the same solution, but that also has a better conditioning. Regularization of a least squares fitting modifies the concept of optimum by penalizing a suitably chosen property of the fitted parameters in addition to making the χ^2 as small as possible.

The slant optical thickness $\tau_{l,j}^{obs} = \tau^{obs}\left(r_{0,j}^{obs}, \lambda_l\right)$ measured at a set of tangent radius $r_{0,j}^{obs}$, $j = 1, \ldots, n_{r_{obs}}$ and wavelengths λ_l, $l = 1, \ldots, L$ provided by a spectrally-resolved instrument staring at the sun through the atmosphere, such as ExoMars-TGO-NOMAD for example, can be packed using one single index aggregating all the observations: $\tau_{j_{obs}}^{obs} = \tau_{l,j}^{obs} = \tau\left(r_{0,j}^{obs}, \lambda_l\right)$ with $j_{obs} = l + (j-1)\,L$. The standard deviation affecting $\tau_{l,j}^{obs}$ can be deduced from the standard derivatives methods to be applied to Eq. (30), allowing to compute the weight $w_{l,j}$ (or $w_{j_{obs}}$) to be given to each observation in a least-squares fitting procedure. The fitting parameters will be defined at a set of altitudes (or radial distances) which may be chosen differently for the gas species and for the dusts, as already proposed in Section 2.1. The fitting basis functions, and their Abel transform will then need to be evaluated at all $\left(r_{0,j}^{obs}, \lambda_l\right)$, i.e. for all values of the j_{obs} index used to pack the observations, so that the χ^2 function is successively written:

$$\begin{aligned}
\chi^2 &= \sum_{j=1}^{n_{r_{obs}}} \sum_{l=1}^{L} \left(\sum_{k=1}^{n_{r_{fit}}} \left(\sum_{i=1}^{n_{sp}} a_k^i \sigma_i(\lambda_l)\, T_k(r_{0,j}) + \kappa_{0,k} T_k^d(r_{0,j}, \lambda_l) \right) - \tau_{l,j}^{obs} \right)^2 w_{l,j} \\
&= \sum_{j=1}^{n_{r_{obs}}} \sum_{l=1}^{L} \left(\sum_{k=1}^{n_{r_{fit}}} \left(\sum_{i=1}^{n_{sp}} a_k^i F_k^{sp,i}(r_{0,j}, \lambda_l) + \kappa_{0,k} F_k^d(\vec{\alpha}, r_{0,j}, \lambda_l) \right) - \tau_{l,j}^{obs} \right)^2 w_{l,j} \\
&= \sum_{j=1}^{n_{r_{obs}}} \sum_{l=1}^{L} \left(\sum_{k_{fit}=1}^{n_{fit}} p_{k_{fit}} F_{k_{fit}}(\vec{\alpha}, r_{0,j}, \lambda_l) - \tau_{l,j}^{obs} \right)^2 w_{l,j} \\
&= \sum_{j_{obs}=1}^{n_{obs}} \left(\sum_{k_{fit}=1}^{n_{fit}} p_{k_{fit}} F_{k_{fit} j_{obs}}(\vec{\alpha}) - \tau_{j_{obs}}^{obs} \right)^2 w_{j_{obs}}
\end{aligned} \tag{35}$$

Where we introduced functions $F_k^{sp,i}(r_{0,j}, \lambda_l) = \sigma_i(\lambda_l)\, T_k(r_{0,j})$ that includes the altitude and wavelength functional dependencies of the gas species, functions $F_k^d(\vec{\alpha}, r_{0,j}, \lambda_l)$ for the dusts, which explicitly reminds the dependency over the α parameter at all relevant fitting altitudes, parameters $p_{k_{fit}}$ that packs together all the linear parameters with index k_{fit} varying from 1 to $n_{fit} = n_{sp}\, n_{r_{fit}}^{sp} + n_{r_{fit}}^d$, and functions $F_{k_{fit}}(\vec{\alpha}, r_{0,j}, \lambda_l)$ that pack the altitude and wavelength dependencies of all the basis fitting functions, gas and dust aggregated (the dust functions being the only ones that explicitly depend on the α parameters). The set of parameters $p_{k_{fit}}$ can be viewed as a vector aggregating the linear parameters $\vec{p} = \left(a_1^1, \ldots, a_{n_{r_{fit}}^{sp}}^1, \ldots, a_1^{n_{sp}}, \ldots, a_{n_{r_{fit}}^{sp}}^{n_{sp}}, \kappa_{0,1}, \ldots, \kappa_{0,n_{r_{fit}}^d}\right)$. The observations are aggregated as one single set as announced above, joining the wavelength and tangent radius dependencies.

For any given set of α_k values, there exists a set of $p_{k_{fit}}$ values of the linear parameters minimizing the χ^2 value of Eq. (35): the ones that nullify all the derivatives of χ^2 with respect to the $p_{k_{fit}}$. This condition produces a linear system of equations for the $p_{k_{fit}}$ that, in principle, can be solved using standard numerical analysis methods such as LU decomposition. The $p_{k_{fit}}$ (all the linear parameters) can then be viewed as functions of the α_k, at the expense of a linear system resolution. Denoting, for the sake of formal conciseness $\mathscr{F}_{k_{fit} j_{obs}} = F_{k_{fit} j_{obs}} \sqrt{w_{j_{obs}}}$ and $\mathscr{L}_{j_{obs}}^{obs} = \tau_{j_{obs}}^{obs} \sqrt{w_{j_{obs}}}$ we define the second member vector $\vec{b}$ and the matrixes U and H of the linear system of this least squares minimization problem by equating the derivatives of the usual χ^2 function with respect to the p_i to zero, all depending on the α_k (kept constant at this stage), and obtain a system of equations for vector $\vec{p}$:

$$\begin{aligned}
&\frac{\partial \chi^2}{\partial p_i} = 2 \sum_{j_{obs}=1}^{n_{obs}} \left(\sum_{k_{fit}=1}^{n_{fit}} p_{k_{fit}} \mathscr{F}_{k_{fit} j_{obs}}(\vec{\alpha}) - \mathscr{L}_{j_{obs}}^{obs} \right) \mathscr{F}_{i j_{obs}}(\vec{\alpha}) = 0 \\
&U_{k,j} = \mathscr{F}_{k,j} \quad H(\vec{\alpha}) = U\, U^+ \quad \vec{b}(\vec{\alpha}) = U^+ \, \overrightarrow{\mathscr{L}^{obs}} \\
&H\, \vec{p} = \vec{b}
\end{aligned} \tag{36}$$

As already warned before, those systems of equations solving an inversion problem are prone to ill-conditioning, which requires modifying the concept of optimum for the sake of regularization. This is generally achieved by adding a suitably chosen matrix to the optimization matrix, H in Eq. (36), thus defining a new system with a better conditioning. It can conceivably be desired limiting the effects of the noise unavoidably affecting the data, so that a regularization that penalizes a derivative of the fitting parameters, seen as a set of discrete values of an altitude-dependent function, can reasonably be adopted. The second derivative of the i^{th} gas specie density (or the dust extinction parameter), discretized as the a_k^i fitting parameter can be evaluated along the lines of, e.g., Hubert et al. [2016], defining $h_k = r_{k+1} - r_k$ ($h_n = h_{n-1}$) and using a simple finite difference scheme (dropping upper index i),

$$\begin{aligned}
&\left.\frac{da}{dr}\right|_k \simeq \frac{a_{k+1} - a_k}{h_k} \\
&\left.\frac{d^2a}{dr^2}\right|_k \simeq \frac{\left.\frac{da}{dr}\right|_k - \left.\frac{da}{dr}\right|_{k-1}}{\frac{1}{2}(h_{k-1} + h_k)} \simeq \frac{2\,a_{k-1}}{h_{k-1}^2 + h_{k-1} h_k} - \frac{2\,a_k}{h_k h_{k-1}} + \frac{2\,a_{k+1}}{h_{k-1} h_k + h_k^2} \quad (1 < k < n) \\
&\left.\frac{d^2a}{dr^2}\right|_{k=1} \simeq \left.\frac{d^2a}{dr^2}\right|_{k=2} \qquad \left.\frac{d^2a}{dr^2}\right|_{k=n} \simeq \left.\frac{d^2a}{dr^2}\right|_{k=n-1}
\end{aligned} \tag{37}$$

Expressions for $k = 1$ and $k = n$ are obtained assuming the second derivative remains constant near the boundaries. Denoting $q_k = 1/(h_{k\text{-}1}^2 + h_{k\text{-}1}\, h_k)$ and $v_k = 1/(h_{k\text{-}1}\, h_k + h_k^2)$, the derivatives are expressed in vector format defining vector $\vec{D}_a$ and matrix $\mathbf{B}_0$ as follows:

$$\vec{D}_a = \mathbf{B}_0\, \vec{a}$$

$$\mathbf{B}_0 = 2 \begin{pmatrix}
q_2 & -q_2 - v_2 & v_2 & & & & \\
q_2 & -q_2 - v_2 & v_2 & & & & \\
 & q_3 & -q_3 - v_3 & v_3 & & & \\
 & & \ddots & \ddots & \ddots & & \\
 & & & q_{n-2} & -q_{n-2} - v_{n-2} & v_{n-2} & \\
 & & & & q_{n-1} & -q_{n-1} - v_{n-1} & v_{n-1} \\
 & & & & q_{n-1} & -q_{n-1} - v_{n-1} & v_{n-1}
\end{pmatrix} \tag{38}$$

Regularization will rely either on minimizing the sum of the squares of the second derivatives, which amounts to

$$D_{0,a}^2 = \vec{a}^{\,+}\, \mathbf{B}_0{}^+ \mathbf{B}_0\, \vec{a} \tag{39}$$

or on minimizing the integral of the square of the second derivative, i.e. the sum of the squares weighted by the spacing between the altitude nodes:

$$\begin{aligned}
&B_{ki} = B_{0ki} \sqrt{h_k} \\
&D_a^2 = \vec{a}^{\,+}\, B^+ B\, \vec{a}
\end{aligned} \tag{40}$$

Matrixes Q_0 and Q, which will be used when computing derivatives

of the regularization term with respect to the a_k, are defined as

$$\begin{aligned} Q_0 &= 2\,B_0^+ B_0 \\ Q &= 2\,B^+ B \end{aligned} \tag{41}$$

A regularization matrix suitable for the set of linear parameters packed in vector $\vec{p}$ in Eq. (36) can be constructed along the same lines by combining matrixes such as B and B_0 in a block-diagonal matrix, each block having a number of elements that corresponds to the number of fitting altitude (and basis fitting functions) used for the a_k^i and the $\kappa_{0,k}$. The corresponding Q matrixes of Eq. (41) will then be block-diagonal as well. Let us denote $\mathscr{Q}$ this grand regularization matrix packing the Q matrixes relevant for all the linear parameters. Regularization will be introduced in the fitting process by assigning a weight to it, based on the properties of the H and $\mathscr{Q}$ matrixes.

The regularized χ^2 expression now includes a term penalizing the second derivative of the linear parameters p_i, which are retrieved by solving the corresponding minimization system having second member vector $\vec{b}$ and Hermitian matrix $\mathscr{H}$, built using the matrix U of the unregularized fitting problem and the regularization matrix $\mathscr{Q}$. Parameter λ is introduced in order to adapt the weight given to the regularization to the properties of the Hermitian matrix H of the unregularized minimization problem, so that the minimization system is expressed as:

$$\begin{aligned} &\chi^2 = \sum_{j_{obs}=1}^{n_{obs}} \left(\sum_{k_{fit}=1}^{n_{fit}} p_{k_{fit}} \mathscr{T}_{k_{fit} j_{obs}}(\vec{\alpha}) - \mathscr{L}_{j_{obs}}^{obs} \right)^2 + c\lambda D_p^2 \\ &\frac{\partial \chi^2}{\partial p_i} = 2 \sum_{j_{obs}=1}^{n_{obs}} \left(\sum_{k_{fit}=1}^{n_{fit}} p_{k_{fit}} \mathscr{T}_{k_{fit} j_{obs}}(\vec{\alpha}) - \mathscr{L}_{j_{obs}}^{obs} \right) \mathscr{T}_{i j_{obs}}(\vec{\alpha}) + c\lambda \mathscr{Q} \vec{p} \\ &U_{kj}(\vec{\alpha}) = \mathscr{T}_{kj} \quad H(\vec{\alpha}) = UU^+ \quad \vec{b}(\vec{\alpha}) = U^+ \overrightarrow{\mathscr{L}^{obs}} \quad \mathscr{H}(\vec{\alpha}) = H(\vec{\alpha}) + c\lambda(\vec{\alpha})\mathscr{Q} \\ &\lambda(\vec{\alpha}) = \frac{Tr(H(\vec{\alpha}))}{Tr(\mathscr{Q})} \\ &\mathscr{H}\vec{p} = \vec{b} \end{aligned} \tag{42}$$

where c is a user-supplied weight, while Tr(A) denotes the trace of matrix A, along the lines of the weighting proposed by Press et al. [1992]. Strictly speaking, the trace is generally not considered a matrix norm. However, it amounts to the sum of the eigenvalues of any (diagonalizable) matrix. From that standpoint, it makes sense using the trace ratio of Eq. (42) in order to balance the importance given to the usual least squares minimization term and to the regularization term. It can also be argued that, as matrixes H and Q are produced by multiplying a matrix U and B, respectively, by its transpose, the traces of H and Q are then the squares of the Frobenius norm of those U and B matrixes, which gives some mathematical grounds to the trace ratio weighting.

As was defined before, regularization penalizes the second derivative of the altitude-dependent linear parameters. If, however, these parameters represent a density, for example, that varies exponentially with altitude, its derivative could be intrinsically large at places, without any effect of noise. It is then preferable to modify the weight given to the regularization by multiplying it by a chosen factor c. The deep goal of regularization remains to protect the method from the ill-conditioning of the linear system to be solved by modifying its set of eigenvalues. Both H and $\mathscr{Q}$ are indeed Hermitian matrixes and can, in principle, be diagonalized using numerical methods, which may fail in the case of H, precisely due to its ill-conditioning.

In the context of the inverse Abel transform fitting of occultation observations through a dusty atmosphere, the H matrix, $\vec{b}$ vector and trace ratio λ all depend on the α_k parameters. And that is where a subtlety arises: Eq. (42) can be viewed as defining the system to be solved in order to retrieve the linear parameters $p_{k_{fit}}$ as functions of the non-linear α_k parameters, while Eq. (35) can be viewed as a definition of the χ^2 to be minimized against the α_k only, the $p_{k_{fit}}$ being themselves functions of the α_k after resolution of the system of Eq. (42). One may even consider adding a regularization term in Eq. (35) that would penalize the variations of the α_k. We will not explicitly include such term here as it only incurs straightforward modifications similar to what was explained above. The non-linear minimization with respect to the α_k then amounts to equating to zero all the derivatives of the χ^2 with respect to the α_k:

$$\begin{aligned} &\chi^2 = \sum_{j_{obs}=1}^{n_{obs}} \left(\sum_{k_{fit}=1}^{n_{fit}} p_{k_{fit}}(\vec{\alpha})\, \mathscr{T}_{k_{fit} j_{obs}}(\vec{\alpha}) - \mathscr{L}_{j_{obs}}^{obs} \right)^2 \\ &\frac{\partial \chi^2}{\partial \alpha_k} = 2 \sum_{j_{obs}=1}^{n_{obs}} \left(\sum_{k_{fit}=1}^{n_{fit}} p_{k_{fit}}(\vec{\alpha})\, \mathscr{T}_{k_{fit} j_{obs}}(\vec{\alpha}) - \mathscr{L}_{j_{obs}}^{obs} \right) \\ &\left(\sum_{k_{fit}=1}^{n_{fit}} \left(\frac{\partial p_{k_{fit}}(\vec{\alpha})}{\partial \alpha_k} \mathscr{T}_{k_{fit} j_{obs}}(\vec{\alpha}) + p_{k_{fit}}(\vec{\alpha}) \frac{\partial \mathscr{T}_{k_{fit} j_{obs}}(\vec{\alpha})}{\partial \alpha_k} \right) \right) \end{aligned} \tag{43}$$

Naturally, among the $\mathscr{T}_{k_{fit} j_{obs}}(\vec{\alpha})$, only those that explicitly depend on the α_k, i.e. the dust functions, will have a non-zero derivative. In contrast, all the $p_{k_{fit}}$ depend on the α_k through matrixes H and U, vector $\vec{b}$ and the trace ratio λ in Eq. (42). The derivatives of the elements of matrix U are computed after the developments of Section 2.1, mostly using Eqs. (24) and (25). The trace of matrix H is equal to the sum of the squares of the elements of matrix U, so that the derivative of λ is easily found:

$$\begin{aligned} &Tr(H) = \sum_j H_{j,j} = \sum_j \left(\sum_i (U^+)_{j,i} U_{i,j} \right) = \sum_{i,j} U_{i,j}^2 \\ &\frac{\partial \lambda(\vec{\alpha})}{\partial \alpha_k} = \frac{2}{Tr(\mathscr{Q})} \sum_{i,j} U_{i,j} \frac{\partial U_{i,j}}{\partial \alpha_k} \end{aligned} \tag{44}$$

The derivative of matrix H and vector $\vec{b}$ can also be obtained from those of matrix U, so that the derivatives of matrix $\mathscr{H}$ can also be computed:

$$\begin{aligned} \frac{\partial H}{\partial \alpha_k} &= \left(\frac{\partial U}{\partial \alpha_k} \right)^+ U + U^+ \frac{\partial U}{\partial \alpha_k} \\ \frac{\partial \vec{b}}{\partial \alpha_k} &= \left(\frac{\partial U}{\partial \alpha_k} \right)^+ \overrightarrow{\mathscr{L}^{obs}} \end{aligned} \tag{45}$$

All the elements needed to compute the derivative of the p_k are now known, and we have successively

$$\begin{aligned} &\mathscr{H}\vec{p} = \vec{b} \\ &\mathscr{H} \frac{\partial \vec{p}}{\partial \alpha_k} = \frac{\partial \vec{b}}{\partial \alpha_k} - \frac{\partial \mathscr{H}}{\partial \alpha_k} \vec{p} \end{aligned} \tag{46}$$

so that, as soon as $\vec{p}$ is known from the resolution of the system of Eq. (42), its derivatives can also be computed solving a system that has the same matrix, a situation particularly suitable for the use of standard resolution methods such as the LU decomposition. It is straightforwardly shown that $\frac{\partial \mathscr{H}^{-1}}{\partial \alpha_k} = -\mathscr{H}^{-1} \frac{\partial \mathscr{H}}{\partial \alpha_k} \mathscr{H}^{-1}$ given that $\mathscr{H}^{-1}\mathscr{H} = I$ (the identity matrix) and that Leibnitz's derivation product rule also applies to matrix multiplication. Formally, the last line of Eq. (46) is then equivalent to

$$\frac{\partial \vec{p}}{\partial \alpha_k} = \mathscr{H}^{-1} \frac{\partial \vec{b}}{\partial \alpha_k} + \frac{\partial \mathscr{H}^{-1}}{\partial \alpha_k} \vec{b} \tag{47}$$

as expected. Computationally, it nevertheless remains preferable using Eq. (46) and avoid explicitly manipulating the inverse of matrix $\mathscr{H}$.

The preceding developments can be used in a method performing the

inverse Abel transform. All the needed function evaluation expressions and their derivatives are available to implement a non-linear least-squares fitting technique, such as the Levenberg Marquardt algorithm [Press et al., 1992], to be ran in a parameter space made as small as possible, i.e. having a number of dimensions as restricted as possible. This reduction of the number of dimensions comes at the expense of more complex derivatives evaluations and linear systems solving, which fortunately all rely on the same matrix. Regularization can be addressed and implemented in a direct manner in order to improve the conditioning of that matrix, with a weight adaptatively applied depending on the matrix trace.

2.4. Exponentially-varying species

In a planetary atmosphere, the gas density varies mostly exponentially with altitude, according to the hydrostatic and diffusive equilibrium laws, with a slope that depends locally on the gas temperature and composition. It is therefore tempting to represent the density profile of the several gas species as piecewise exponential functions, instead of piecewise linear functions as was done above, even for minor species (such as O_3) although it is expected to reach an extremum owing to its photochemistry, where it can depart from the exponential function, even locally.

Let us consider a function f(r) assumed to have strictly positive values ϕ_k at a set of discrete radial distances r_k. This function can be approximated using exponential pieces matching those discrete values, and their Abel transforms and derivatives can also be computed. Denoting a_k and b_k the parameters of the exponential function used to represent the ϕ_k between r_k and r_{k+1}. Those parameters are directly computed from the r_k and ϕ_k, so that the exponential pieces f_k and their Abel transform F_k can be expressed. Function f being the sum of the f_k, its Abel transform F is then the sum of the F_k, and all the derivatives with respect to the ϕ_k, which are required for non-linear fitting purposes, follow naturally:

$$
\begin{aligned}
&f(r) = \sum_{k=1}^{n-1} a_k exp(b_k\,(r - r_k))\,\chi_{[r_k, r_{k+1}[}(r)\\
&f(r_k) = \phi_k \quad f(r_{k+1}) = \phi_{k+1}\\
&a_k = \phi_k \qquad b_k = \frac{ln\left(\frac{\phi_{k+1}}{\phi_k}\right)}{r_{k+1} - r_k}\\
&f(r) = \sum_{k=1}^{n-1} f_k(r) : f_k(r) = \phi_k \left(\frac{\phi_{k+1}}{\phi_k}\right)^{\frac{r-r_k}{r_{k+1}-r_k}} \chi_{[r_k, r_{k+1}[}(r)\\
&F(r_0) = 2\int_{r_0}^{\infty} \frac{r}{\sqrt{r^2 - r_0^2}} f(r)\,dr = \sum_{k=1}^{n-1} F_k(r_0)\\
&F_k(r_0) = 2\int_{r_k^*}^{r_{k+1}^*} \frac{r}{\sqrt{r^2 - r_0^2}} f_k(r)\,dr = 2\int_{\sqrt{r_k^{*2} - r_0^2}}^{\sqrt{r_{k+1}^{*2} - r_0^2}} f_k\left(\sqrt{y^2 + r_0^2}\right)\,dy\\
&\frac{\partial f_k(r)}{\partial \phi_k} = \left(1 - \frac{r - r_k}{r_{k+1} - r_k}\right)\left(\frac{\phi_{k+1}}{\phi_k}\right)^{\frac{r-r_k}{r_{k+1}-r_k}} \chi_{[r_k, r_{k+1}[}(r)\\
&\frac{\partial f_k(r)}{\partial \phi_{k+1}} = \frac{r - r_k}{r_{k+1} - r_k}\,\phi_k^{1 - \frac{r-r_k}{r_{k+1}-r_k}}\,\phi_{k+1}^{\frac{r-r_k}{r_{k+1}-r_k} - 1}\,\chi_{[r_k, r_{k+1}[}(r)\\
&\frac{\partial F_k(r_0)}{\partial \phi_{k+1}} = 2\int_{\sqrt{r_k^{*2} - r_0^2}}^{\sqrt{r_{k+1}^{*2} - r_0^2}} \frac{\partial f_k\left(\sqrt{y^2 + r_0^2}\right)}{\partial \phi_{k+1}}\,dy
\end{aligned}
\tag{48}
$$

where again $r_k^* = max(r_k, r_0)$ and substitution $y = \sqrt{r^2 - r_0^2}$ has been used, which gets rid of the singularity of the Jacobian of the Abel transform near the tangent radius r_0. Abel transforms F_k of the exponential pieces f_k of Eq. (48) can be computed analytically (as far as incomplete gamma and exponential integral functions can be considered analytic) using the non-alternating series development proposed by Hubert et al. [2022], or using a numerical integration, which these authors also recommend as computationally less expensive.

In the context of inversing the Abel transform of the optical thickness of the atmosphere, determined by occultation of the sun, the ϕ_k of Eq. (48) represent the estimated gas density $[g_k^i]$, and as many f_k and F_k functions must be defined as gas species are included in the treatment. They will be denoted with an upper index, f_k^i and F_k^i. The χ^2 is then expressed as

$$
\chi^2 = \sum_{j=1}^{n_{r_{obs}}} \sum_{l=1}^{L} \left(\sum_{k=1}^{n_{r_{fit}}} \left(\sum_{i=1}^{n_{sp}} \sigma_i(\lambda_l)\, F_k^i(r_{0,j}) + \kappa_{0,k} T_k^d(r_{0,j}, \lambda_l) \right) - \tau_{l,j}^{obs} \right)^2 w_{l,j}
\tag{49}
$$

to which a regularization term can again be added. Deriving the χ^2 with respect to all the fitting parameters can be done using the formulas given above. Again, it can also be convenient packing all the observations using one single index to enumerate the pairs $r_{0,j}$, λ_l. Determining the gas densities and dusts properties can then be considered using a general non-linear least squares fitting method such as the Levenberg-Marquardt algorithm. We anticipate here over the next section and state that obtaining an algorithm performing the fitting with the assumptions made in this paragraph is difficult. The problem is non-linear with respect to the gas species densities (as well as the dust α parameter) and the number of dimensions of the space in which the optimum is searched becomes large. As far as we could test, the fitting requires a very good first guess that may be provided using the method presented in Section 2.3, but it is not clear including the exponential dependency will improve the fitting. Indeed, using exponential elements requires imposing the fitted densities remain all positive, whereas the other method tolerates negative densities. These negative values are naturally non-physical, but this gives the fitting method additional freedom, seemingly allowing a better fitting and a better determination of all fitting parameters over most of the altitude range. We suspect, although we could not establish it formally, that the higher degree of nonlinearity introduced here can result in the χ^2 function having more local extrema, therefore implying that a very good first guess must be provided.

3. Numerical methods and validation

3.1. Test case properties

Performing the inverse Abel transform fitting of occultation observation of a dusty atmosphere requires a non-linear method, owing to the wavelength dependence of the dusts extinction. Several algorithms exist for minimization in a multidimensional space, including the Levenberg-Marquardt method [Press et al., 1992], which avoids explicit computation of the Hessian matrix using a numerical approximation for the second derivative of the function. The Nelder and Mead down-hill simplex method can also be considered, but it implies a large number of function evaluations, especially when applied in a parameter space that has many dimensions. For example, if the α parameters must be determined at 40 altitudes, the corresponding parameter space will have 40 dimensions, and the number of nodes of the moving simplex of the algorithm will reach 41. This will unavoidably lead to heavy computations.

The simplest method proposed in Section 2.2 separates the inversion and parameters fitting, so that a first least squares fitting is needed for the inverse Abel transform (at all wavelengths), followed, at each fitting altitude (i.e. for each r_k), by a second least squares fitting which remains non-linear with respect to one single parameter only. This is clearly the computationally fastest method one may consider.

To test different methods, we will use a fictitious case of atmosphere observation having realistic prescribed CO_2 and O_3 densities, with dust properties vertical profiles resembling observational results given by

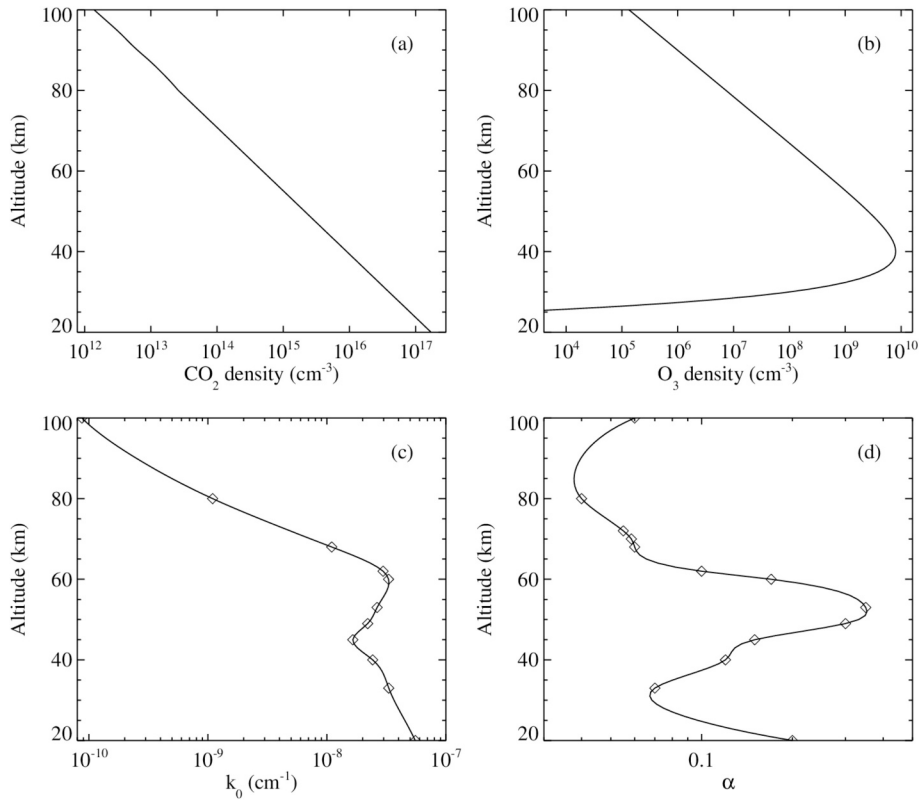

Fig. 2. Atmospheric vertical profiles used for method testing. CO_2 and O_3 densities are shown in panels (a) and (b) respectively. Panel (c) shows the dust extinction coefficient at reference wavelength $\lambda_0 = 250$ nm, while panel (d) gives the vertical profile of the dusts α parameter. The diamonds of panels (c) and (d) show the small set of reference discrete values used to build the vertical profiles at all altitudes using cubic spline interpolation.

Määtänen et al. [2013], presenting numerically challenging characteristics, such as local extrema and variation across a broad range of values. We will test the method with and without noise included. It is expected that, when no noise is included, any reliable inversion method should retrieve the prescribed atmospheric properties with a reasonable accuracy, but not necessarily exactly, since the inversion method includes a regularization term. Fig. 2 shows the atmospheric properties used for testing purposes. The CO_2 density is from Krasnopolski [2002] extended to low altitudes under an isothermal hypothesis, the detail of the profile being not crucial for the sake of method testing. The O_3 density profile is build using a Chapman profile with properties compatible with Lebonnois et al. [2006], with a scale height of 5 km and a peak density of 8×10^9 cm^{-3} at 40 km of altitude. The dust properties are interpolated at all altitudes using cubic spline interpolation of discrete values taken from a profile by Määttänen et al. [2013], artificially completed at high altitude. The detailed values are indeed of little importance as far as they are representative of what can be expected in the Mars atmosphere and present a sufficient complexity to challenge the method (i.e. broad range of variation, local extrema). We avoid using extremely small values of the dusts α parameter at high altitude, as it would imply nearly no dependency on wavelength, and it is not expected a fitting method should retrieve the exact value of a parameter over which the observation is nearly not sensitive, especially if the problem is somewhat ill-conditioned. The solar spectrum used to create simulated occultation data is taken from the Solar 2000 model [Tobiska et al., 2000].

Fig. 3 shows the attenuation of solar radiation at 285 nm occulted by the Mars atmosphere given in Fig. 2. The presence of local minima in the density of an absorber or in the extinction coefficient of the dusts can lead to a counter-intuitive shape of the attenuation. As the line-of-sight tangent point passes under the altitude of the local O_3 extremum, a significant portion of the l.o.s. near the tangent point passes through an atmosphere layer nearly devoid of O_3, so that the length of the l.o.s. segments through which significant O_3 absorption takes place is severely reduced, as it can be understood considering the geometry of Fig. 1 and lines-of-sight of different tangent altitude passing through a thin spherical shell of absorbing material. The simulated profile is vastly dominated by dust absorption, while CO_2 plays a minor role. If, however, dust attenuation were severely smaller and could be neglected, CO_2 absorption may become locally dominant for l.o.s. tangent altitudes below ~25 km, i.e. a few scale heights below the O_3 peak density. Only a small fraction of the solar radiation is however expected to reach such a low altitude. The dust, O_3 and CO_2 optical thickness shown in Fig. 3, suggest that, at lower wavelengths, CO_2 may play a major role in the bottom side of the profile. The solar flux does, however, severely decrease at short UV wavelength and exp.(−3) is already 0.05: a division by 20, so that few photons would reach the detector of an instrument observing at short wavelength and low tangent height. As it will be discussed in Sections 4 and 5, retrieving the CO_2 density from occultation observation in this wavelength range remains very challenging. The peak of the O_3 optical thickness is conspicuous. It corresponds to the maximum of the Hartley band cross section and to the maximum of the ozone density profile. The combined dependency of the dust extinction parameter with respect to altitude and wavelength is apparent in the optical thickness as well, but from a relative standpoint, the 200–300 nm wavelength range clearly offers the best sensitivity to ozone. It can also be expected that the very tenuous atmosphere of the topside will generally not make it possible retrieving the profiles and properties of the constituents from occultation data, the optical thickness remaining too close to 0 for producing very significant attenuation of the solar flux of UV photons.

3.2. *Two-steps inversion*

We first consider the inversion method proposed in Section 2.2., i.e.,

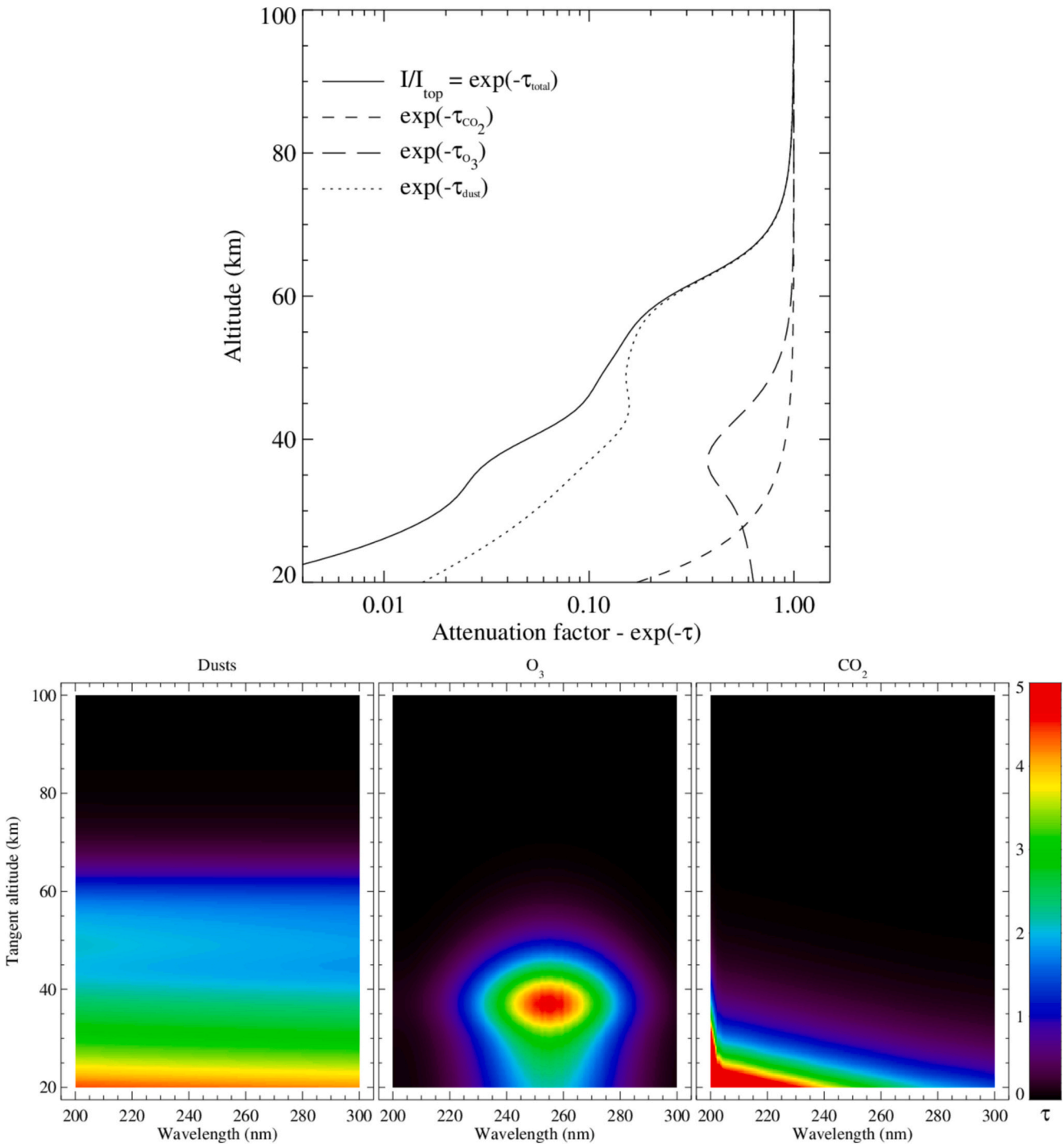

Fig. 3. Attenuation of the solar radiation at 285 nm as a function of tangent point altitude, under occultation through the Mars atmosphere, simulated using the atmosphere characteristics shown in Fig. 2 (top panel). The contributions of the dusts, CO_2 and O_3 are explicitly given. Local extremum of an absorber can lead to a local minimum in the attenuation factor vertical profile. Attenuation optical thickness of the dusts, ozone and CO_2 in the 200–300 wavelength range for lines of sights having their tangent height ranging from 20 to 100 km (bottom panels).

the total optical thickness (or extinction coefficient) is obtained at each wavelength and tangent radius by computing the opposite of the logarithm of the ratio of the attenuated intensity over the unattenuated (i.e. topside) intensity. The local, differential extinction coefficient is obtained by inverse Abel transform of the l.o.s. -integrated extinction coefficient, at each wavelength, for a set of fitting altitudes (or radial distances), then, at each fitting altitude, the wavelength-dependent local differential extinction coefficient is used to fit the dusts properties and the absorbing gas densities. The results obtained when no noise is included in the test are shown in Fig. 4. The differences between the original input profiles and the inversion-retrieved profiles are imperceptible except for the bottom-side of the O_3 density profile. In that domain of altitudes, the ozone density rapidly drops, while the simulated intensity is already strongly extinguished. The ozone retrieval is therefore less accurate (in a relative sense). The inversion was performed giving a very small weight to the regularization, as there is no point in trying to accommodate the effect of noise here. Increasing the weight of regularization can, indeed, degrade the quality of the retrieval,

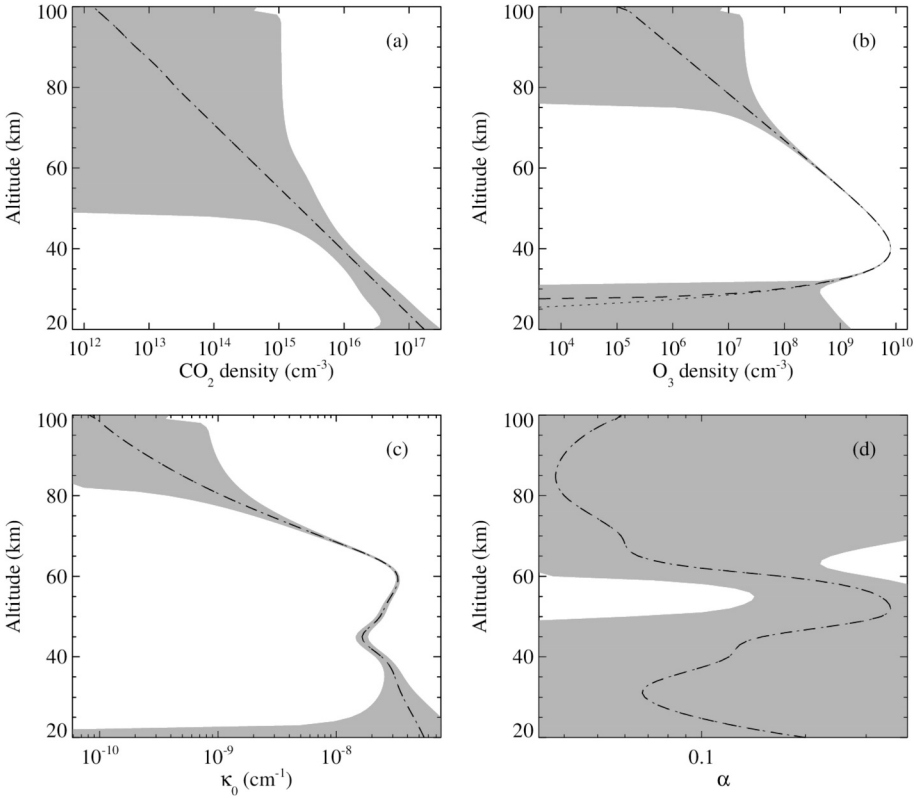

Fig. 4. Atmospheric properties retrieved using the two-steps inversion method of Section 2.2, applied to simulated observations described in Section 3.1., without including any noise. Panels (a), (b), (c) and (d) show the results for the CO_2 density, O_3 density, dusts extinction coefficient at reference wavelength κ_0 and dusts α parameter, respectively. The dotted lines show the input profiles of the test, while the dashed lines show the inversion-retrieved profiles. The grey shades indicate the ± 1-σ confidence interval that would be obtained owing to a realistic noise level, if applied.

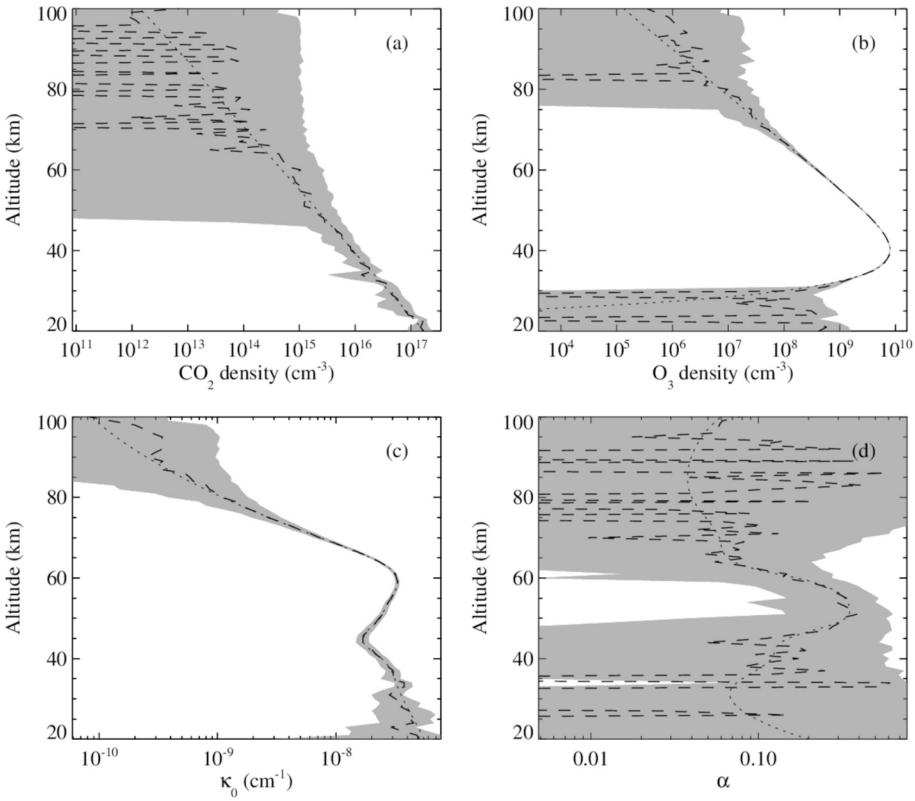

Fig. 5. Same as Fig. 4 when including a realistic noise level in the simulated occultation.

as expected since regularization modifies the concept of optimum. It is therefore also not surprising that the bottom-side O_3 profile cannot be perfectly retrieved at levels a few orders of magnitude lower than the O_3 peak density. A confidence interval was estimated giving some reasonable weight to the simulated pseudo-observations. A signal of 5000 count was assumed at 200 nm on the very top side, and scaled according to the solar flux obtained from the Solar2000 model [Tobiska et al., 2000], the test being conducted using a wavelength interval ranging from 200 to 300 nm. Assuming a Poisson noise then gives a reasonable standard deviation. A noisy disturbance of the simulated pseudo-observation is however not applied here: the goal is to figure out what the confidence interval would look like. Large uncertainties can be expected concerning the α parameter and retrieval of all parameters is less accurate in the altitude range where little extinction occurs, either because the atmosphere is too tenuous (i.e. on the top side) or because the solar UV flux has become too weak and there remain too few photons to characterize the extinction (i.e. on the bottom side).

Fig. 5 shows the inversion results, retrieved using the two-steps method when noise is included in the test. The deleterious effects of noise obviously appear when comparing Fig. 4 and Fig. 5. The different parameters are well retrieved in altitude ranges where the occultation is sufficiently sensitive to that parameter. The CO_2 density is poorly retrieved at high altitude, ozone is still retrieved in an altitude range that corresponds to several orders of magnitude of variation of its density, compared with its peak value. In the altitude ranges where noise severely degrades the retrieval of the gas densities, unrealistic negative values can even be found. This is not surprising considering that those densities are poorly retrieved at altitudes where they are relatively small, some 2–3 orders of magnitude below the peak density in the case of ozone. The reference extinction coefficient of dusts, κ_0, remains well retrieved as well, with poorer reliability on the topside and at very low altitude. In contrast, the alpha parameter is only retrieved in the altitude range where the dusts produce an important attenuation of the simulated intensity and where this intensity remains sufficiently high, so that the overall minimization problem remains sensitive to the parameter. We verified that, after the local, total differential extinction coefficient is correctly retrieved by inverse Abel transform, the second step non-linear fitting of the alpha parameter at each fitting altitude relies on a rather flat χ^2 function near the optimal α. It is therefore expected that noise can degrade the retrieval of the α parameter. Moreover, when the absolute value of the α parameter is small, it introduces a nearly negligible wavelength dependency, so that finding an offset value for alpha makes little difference as long as the parameter remains small. The test was conducted here using a wavelength range from 200 to 300 nm, where ozone has a major absorption band, with a resolution of 1 nm. We verified that extending this range to longer wavelengths, up to 350 nm, for example, does improve the retrieval of the α parameter, without allowing a complete, reliable retrieval over the whole profile. This is not surprising, since introducing more observations naturally reduces the uncertainties over any fitting parameter, and since, in the 300–350 nm wavelength range, the dusts extinction dominates over the ozone absorption, which becomes inexistant beyond ~300 nm. It remains that noise degrades information and therefore the retrieval quality.

It can be concluded from the previous paragraphs and figures that the two-steps fitting method can be considered to realize a quick fitting of the atmospheric properties. Its reliability naturally depends on the noise level contaminating the observation. Its main weakness is that it does not easily allow estimating uncertainties over the fitted parameters. In particular, it cannot explicitly account for covariance between the fitting parameters in the error propagation process. A bootstrapping method for uncertainties estimate was not considered given that it would require heavy computations, making it less attractive for real applications over a broad database, but the possibility remains to use the result of the two-steps method as a first guess for another, more sophisticated general method that provides the uncertainties. The reliability can nevertheless be appreciated in Fig. 5 by comparing the input, known profile (the "truth") represented by the dotted lines and the fitted values shown by the dashed lines. The parameter which is the harder to estimate remains the dusts α parameter, for reasons explained in the previous paragraph.

3.3. Coupled linear-nonlinear method

We now turn to testing of the method described in Section 2.3. It is said to be a coupled linear-nonlinear method as the minimization problem is considered as only depending on the dusts α_k parameters, while all the other relevant fitting parameters are found, for given α_k, by solving the corresponding linear least squares problem, with regularization included to cope with the ill-conditioning of the problem. Regularization over the α_k can also be included to the non-linear fitting method (Levenberg-Marquardt, for example) by including additional equations to the fitting problem. These additional equations correspond to a numerical evaluation of the second derivative of the α_k (with respect to altitude) to be equated to zero, in a least squares sense. A very accurate estimation of those derivatives is not required as the goal is only to penalize noisy variations of the fitted parameters, while improving the conditioning of the optimization Hermitian matrix. Applying a weight to the regularization of the α_k is not straightforward, but it should remain reasonably small as to avoid giving the false feeling of a reliable smooth estimate of the α profile, while it would only reflect the penalization of the derivative rather than a physically accurate estimate of parameter values. As already stressed above, regularization inherently modifies the concept of optimum. The strategy that was followed to reduce the needed computational time is to process the inversion over a restricted set of wavelengths and provide the estimated α profile as an input for a second pass of the fitting procedure using the whole wavelength interval. Indeed, computing the derivative of the matrix elements with respect to all the α_k remains computationally intensive. In return, the number of dimensions of the space over which the non-linear fitting algorithm must search for an optimum is drastically reduced.

Fig. 6 shows the result of the inversion realized using the coupled linear-nonlinear method. A wavelength interval ranging from 200 to 300 nm was used, with a 1 nm resolution. Each simulated pseudo-observation was assigned a weight corresponding to a realistic noise level as explained above regarding Fig. 4. At this stage, no noise was applied to the simulated pseudo-observation and the noise level is only used for the sake of weighting and confidence interval estimate. The grey shades then show the 1-σ confidence interval that can be expected from the fitting. Those intervals are of little significance since no noise was explicitly applied, but they reveal what can be expected from the inversion method. Without a surprise, the inversion closely retrieves all the parameters, except in altitude ranges where the problem is weakly sensitive to the values of the parameters. In the case of the ozone profile, the bottom side is poorly retrieved as the gas density rapidly drops at low altitude while most of the photons have already been absorbed at higher altitude. The use of logarithmic scales allows to appreciate the efficiency of the method over several orders of magnitudes, but it must however be warned that they are also somewhat misleading concerning the method reliability as they make dramatically appear inaccuracies over insignificantly small quantities. The dust properties are again retrieved in a very satisfactory manner, but the broad width of the uncertainties over the α parameter suggests that retrieving its value is challenging when a reasonably large noise is applied to the simulated intensities. Along the same lines, it appears that retrieving the CO_2 density may reveal challenging as well, especially at high altitude.

Introducing a realistic noise in the test naturally degrades the quality of the retrieval as it appears in Fig. 7, although a slight smoothing was applied to the simulated noisy intensities prior to proceeding to the inversion algorithm. It is also conspicuous that the estimated uncertainties provide a very pessimistic evaluation of the fitting reliability of the inversion method, especially for the absorbing gases concentrations and for the dusts κ_0. The dusts α parameter is again the harder to

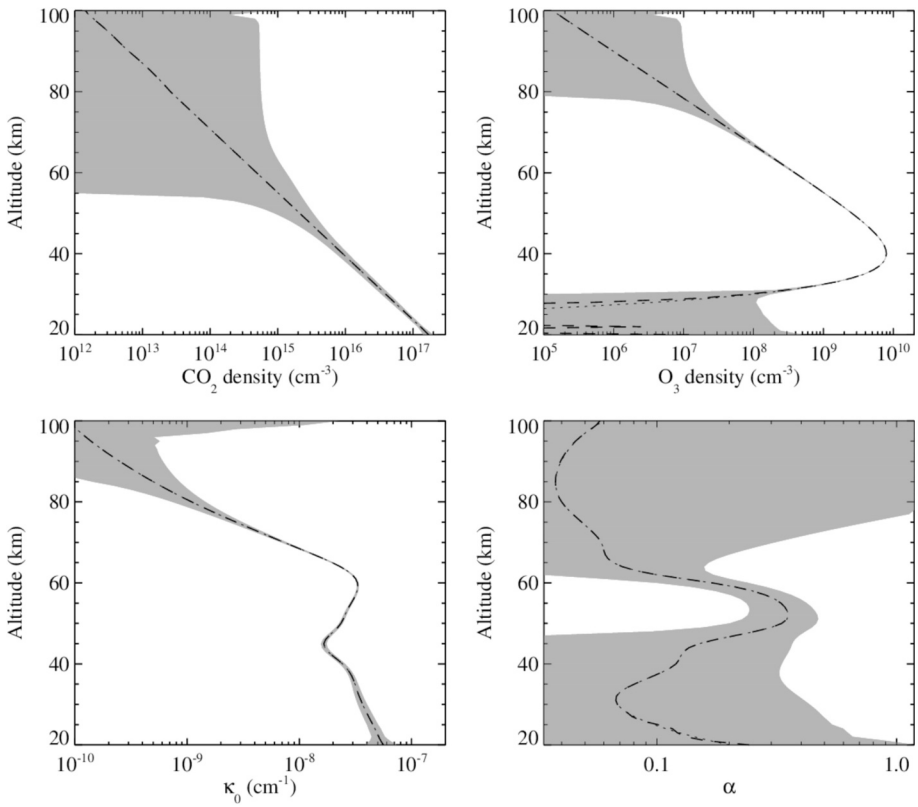

Fig. 6. Atmospheric properties retrieved using the coupled linear – non-linear inversion method of Section 2.3, applied to simulated observations described in Section 3.1., without including any noise. Panels (a), (b), (c) and (d) show the results for CO_2 density, O_3 density, dusts extinction coefficient at reference wavelength κ_0 and dusts α parameter, respectively. The dotted lines show the input profiles of the test, while the dashed lines show the inversion-retrieved profiles. Grey shades show the ± 1-σ confidence interval of the fitted parameters.

retrieve. The uncertainties affecting its value nevertheless remain exaggeratedly large.

The retrieval of the α parameter profile can be improved by extending somewhat the wavelength interval over which the fitting is performed, as shown in Fig. 8 giving the result of the inversion test realized over a wavelength range from 200 to 350 nm. Including more spectrally extended data naturally improves the knowledge of the system, and in this particular case, the improvement is brought in a wavelength range where ozone is not expected to largely contribute the occultation. The estimated uncertainties are rather large, given that the retrieved parameters, especially the linear parameters (gas concentrations and differential dust extinction coefficients), remain quite close to the input "truth" represented by the dotted lines over a significant portion of the vertical profiles. As already mentioned, the topside and bottom-side values remain the hardest to retrieve because the atmosphere is scarce on the top side and produces little absorption while the attenuated solar flux is small on the bottom side, leaving few remaining photons to be absorbed. The retrieval of the α_k is also somewhat better. In particular, the α parameter is better retrieved below ~45 km of altitude, down to ~32 km of altitude. The topside of the retrieved profile is less noisy, and fairly reliable up to ~75 km. The improvement is however obtained at the expense of a somewhat longer computational time, and noisy, spurious variations remain important on the very top and bottom sides. Their amplitudes appear less severe, though. The ozone peak appears to be perfectly retrieved, with negligible uncertainties affecting the O_3 and κ_0 parameters over most of the vertical profile, over which a nearly perfect agreement is found with the dotted "true" profiles. The very topside of the ozone density profile appears also better retrieved in Fig. 8 than in Fig. 7, but the ± 1-σ interval is so broad that the improvement can hardly be considered significant. Retrieving the CO_2 concentration remains difficult at high altitudes, the product of its density and extinction cross section being very small at high altitude in this test case.

We also attempted to increase the weight given to the regularization applied to the α parameter profile to produce a smoother result, apparently closer to the expected "truth" (the dotted lines). It is found that the shape of the noisy portion of the retrieved profile does not appear to be better nor worse than what is shown in Fig. 8. The interest of regularization remains to protect the inversion method against ill-conditioning: it is, by conception, not able to intrinsically reduce the difference between the fit and the observation. At best can it somewhat dampen noisy variations, which would otherwise be larger owing to ill-conditioning. As the regularization method used here relies on the local evaluation of second derivatives, a too large weight given to the regularization can even become counter-productive, since exponentially-varying quantities (such as gas concentrations in a planetary atmosphere) have large derivatives when those quantities are large.

The coupled linear-nonlinear method appears as a valid method to invert occultation observations of a dusty atmosphere. Comparing its results with those shown in Section 3.2, it also appears preferable as the uncertainties over the profiles appear to be less. Both sets of retrieved profiles remain quite comparable, however. Computationally, the coupled linear-nonlinear method is more expensive, but it also provides an estimate of all the atmospheric parameters in a unique fitting process, which includes possible interdependence and covariance between the parameters determined at different altitudes.

3.4. *Exponentially-varying gas species*

Tests similar to those of Sections 3.2 and 3.3 have also been conducted using a fully non-linear method adjusting simultaneously the dusts properties and the gas density profiles assuming gas concentration

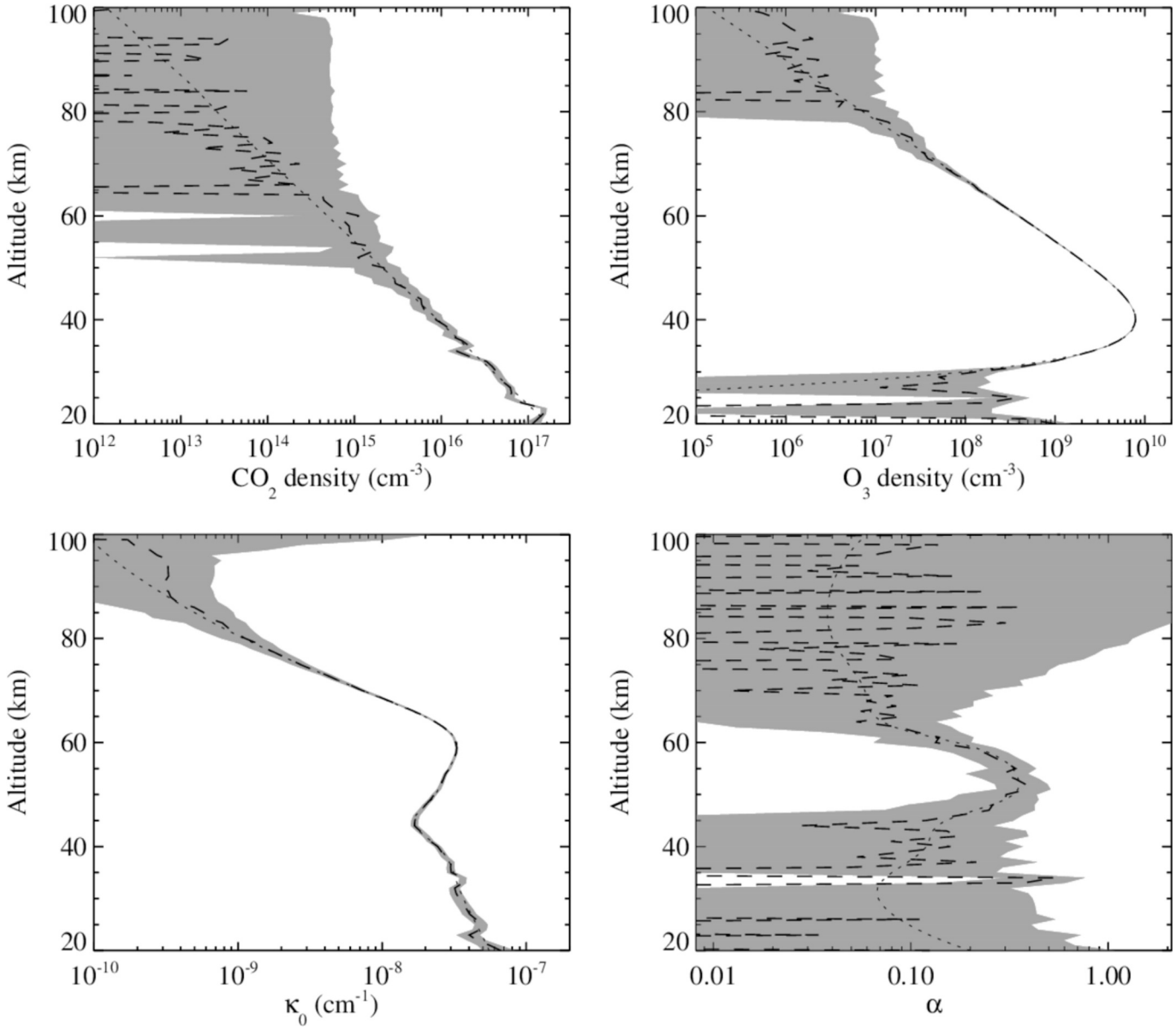

Fig. 7. Same as Fig. 6, with a realistic noise applied to the simulated occulted intensities. A wavelength range extending from 200 to 300 nm was used.

varies exponentially between fitting altitudes, i.e. using the formalism developed in Section 2.4. The least squares fitting process is by far more complex, since all parameters are considered non-linear (even the aerosol extinction parameter), so that the number of dimensions of the parameter space explored by the Levenberg-Marquardt algorithm is multiplied by 4. This increased complexity results in longer computational time, and less efficient retrieval of the sought atmospheric properties.

Fig. 9 shows the inversion-retrieved profiles of the gas densities and dust properties. As already done above, the ±1-σ confidence intervals represented by the grey shades reflect the noisy variations that could be expected if a realistic noise had been included. The method can hardly retrieve the proper atmospheric properties on the very top side, as well as the α parameter on the bottom side of the profile. Fitting convergence is indeed harder to achieve in this case for the reasons explained above (stronger non-linearity, larger number of dimensions of the parameters space), especially in altitude ranges where the simulated pseudo-observations are only weakly dependent on the atmospheric properties.

Fig. 10 presents the results obtained when a realistic noise is included in the simulated occulted intensity profile. The noisy degradation of the retrieved parameters is conspicuous, especially on the top side. The α parameter is again the harder to retrieve. Its assumed relatively low value implies a weak simulated dependency of the dust extinction with respect to wavelength. It is therefore logical that this parameter remains difficult to estimate in this case as well.

3.5. *Statistical evaluation*

The three methods presented in the previous paragraphs show a common feature when noise is included in the test simulations. The retrieved dusts extinction parameter (at reference wavelengths of 250 nm) presents a similar overestimate on the topside in each case. It can be wondered if this overestimate is incidentally inherent to the specific noise distribution that was adopted in the present simulation. We therefore conducted a statistical test simulating 1000 noise distributions to be added to the same simulated count rates to be inverted. This test being computationally intensive, it was not conducted using the method of Section 2.4.

Fig. 11 presents the statistical properties of the inversion of the simulated noisy occultation profiles, using the coupled linear –

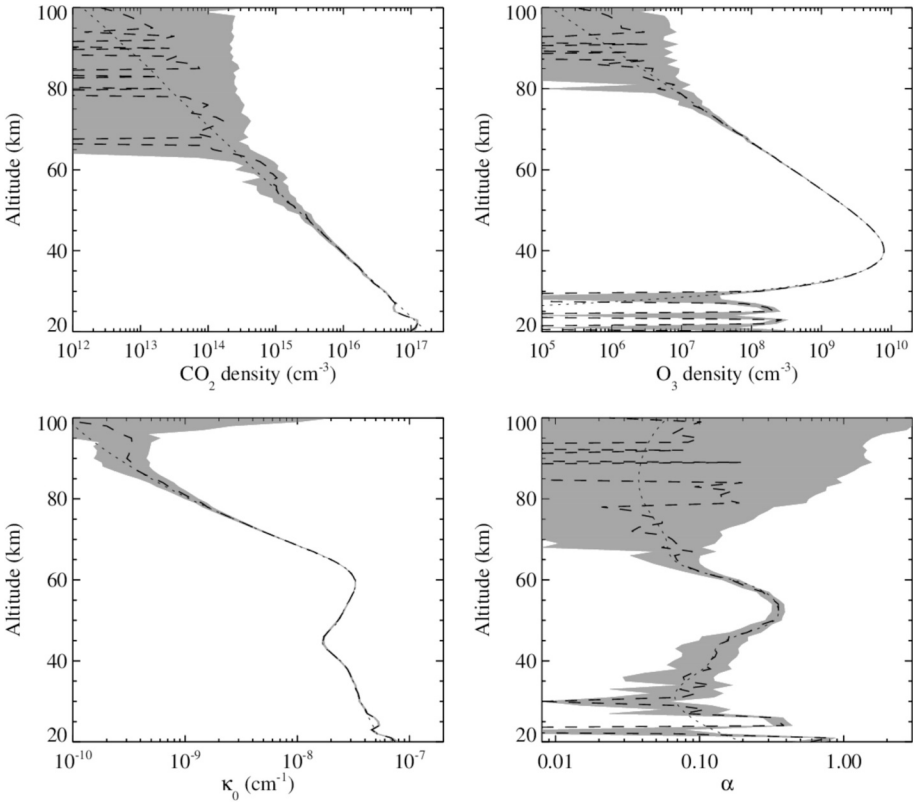

Fig. 8. Same as Fig. 7, using a wavelength range from 200 to 350 nm.

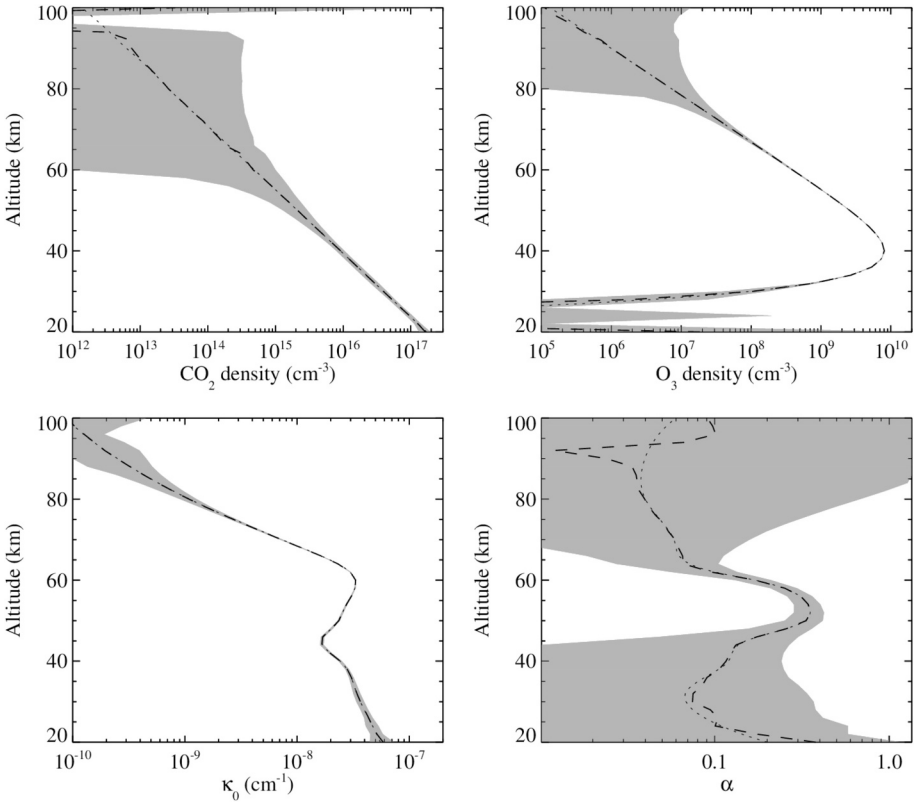

Fig. 9. Atmospheric properties retrieved using a Levenberg-Marquardt fitting applied to the simulated observations described in Section 3.1., without including any noise, using the functional dependencies described in Section 2.4, i.e. assuming the gas density profiles are locally exponential. Panels (a), (b), (c) and (d) show the results for CO_2 density, O_3 density, dusts extinction coefficient at reference wavelength κ_0 and dusts α parameter, respectively. The dotted lines show the input profiles of the test, while the dashed lines show the inversion-retrieved profiles. Grey shades show the ± 1-σ confidence interval of the fitted parameters.

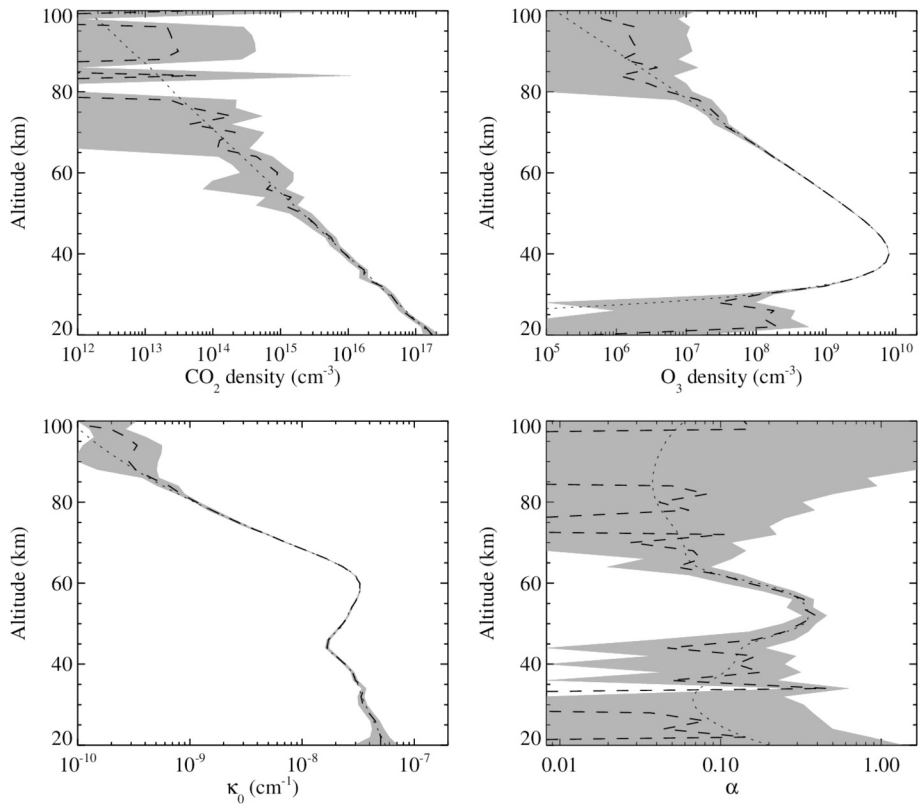

Fig. 10. Same as Fig. 9, with a realistic noise applied to the simulated occulted intensities. A wavelength range extending from 200 to 300 nm was used.

nonlinear method of Section 2.3. It appears that the confidence intervals estimated in Fig. 7 match the statistical testing rather well. This is noticeable, given that the standard methods generally used to estimate uncertainties rely on the assumption that the data follow a Gaussian distribution. This assumption can hardly be considered strictly valid, since, in the case of occultation observations, inversion is applied to the logarithm of the (simulated) intensity, which provides an estimate of the total extinction optical thickness at all wavelengths. Surprisingly, the topside of the (differential) extinction coefficients of the dusts at 250 nm determined by the inversion process is significantly larger than the expected "true" value shown by the dotted lines. For all other parameters, the "true" dotted line profile is bracketed by the ±1-σ interval about the mean. It therefore appears that, at least as far as the aerosols are concerned, the effect of noise contamination of the (simulated) observations is not only to introduce a scatter on the retrieved profiles, but also to introduce a bias, especially in altitude ranges where the observed intensity profile only weakly depends on the properties of the atmosphere.

As expected, the confidence interval of the α parameter becomes large in altitude ranges of low sensitivity (i.e. the upper and lower parts of the profile). The noisy nature of the retrieved α profile shown in the previous sub-sections can therefore be attributed to the very noisy nature of the (simulated) observations, rather than to a serious defect of the retrieval methods. We nevertheless investigate possible subtleties that may result from the fitting algorithm.

The Levenberg-Marquardt method combines the conjugate gradient method with a quasi-Newton method, giving more and more weight to this latter as the algorithm approaches the optimum. Quasi-Newton methods approximate the function to be minimized, i.e. the χ^2 function, with a multi-dimensional second-degree function, replacing the actual Hessian matrix, by a pseudo-Hessian matrix computed based on first derivatives only. As emphasized by Press et al. [1992], the optimum of the merit function is identified by nullifying its first derivatives, and it does not much matter what path in parameter space is followed by the algorithm to reach and satisfy that condition, so that using an approximate Hessian generally fits the need as well as the exact Hessian matrix would. It is then implicitly assumed that any point satisfying a zero-gradient condition will do as an optimum point. We estimated (numerically) the exact Hessian matrix near the optimum, for a very limited number of cases owing to the extreme computational cost this incurs. It is found that, although the pseudo-Hessian has only positive eigenvalues (which would point at a true extremum), the exact Hessian matrix evaluated at the estimated optimum has a few negative eigenvalues of relatively small absolute value. This indicates that, in the particular case of inverse Abel transform fitting, the Levenberg-Marquardt algorithm (and very likely any quasi-Newton algorithm) may stop at a saddle point instead of a true extremum. We are not aware of any other fitting problem presenting a similar issue. We however point out that the two-steps method presented in Section 2.2 and tested in Section 3.2 leads to fairly similar results as the coupled linear-nonlinear method, whereas the nonlinearity of the fitting with respect to the α parameter is addressed in the two-steps method using a one-dimensional bisection method, which is not subject to any confusion between a saddle point and an extremum. Although we could not prove it, we suspect that the confusion between a saddle point and an extremum occurs here because the (simulated) intensity is only weakly dependent on some of the parameters, especially on the topside α values. If however, it should appear that, for a given optimization problem, such an optimum mis-attribution would become critical, another fitting method may need being applied. This may include the Nelder-Mead down-hill simplex or a simulated annealing method [Press et al., 1992], or even a particle swarm optimization (PSO) technique [e.g. Banks et al., 2007; 2008] or any other stochastic method. Those methods are however known to be very expensive from a computational standpoint, which makes them less usable for the analysis of large datasets. It must be added that the different fitting parameters covary to various extent in this fitting problem, parameters obtained at nearby altitudes influencing each other more efficiently than very distant ones. It can then be also considered that opposite deviations of the gas densities and

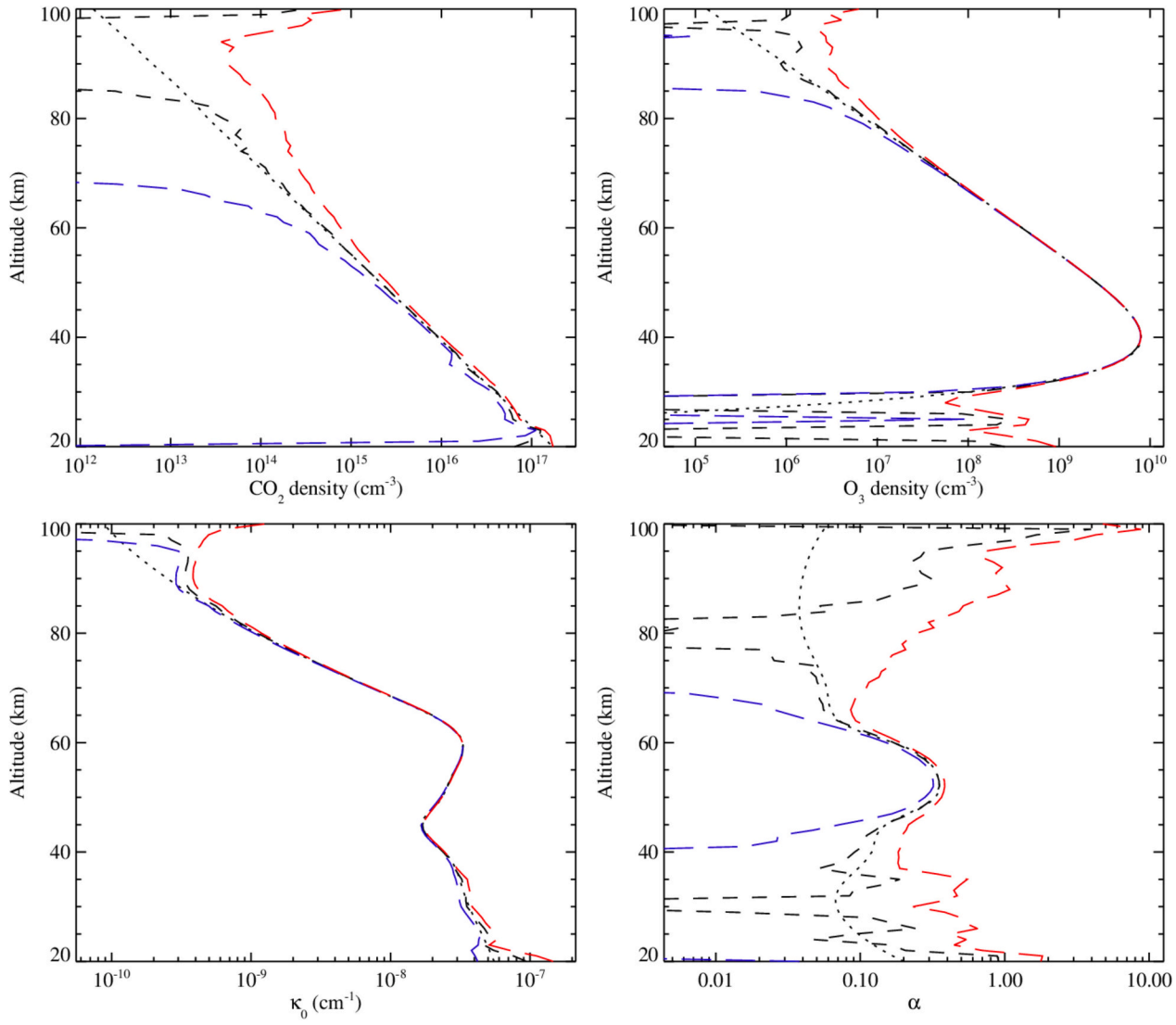

Fig. 11. Synthesis of inversions of 1000 simulated noisy occultation profiles. The dotted lines represent the input (noise-free) profiles to be retrieved. The black dashed lines represent the average of the 1000 retrievals. The red and blue dashed lines bracketing the black one show the ±1-σ interval of the retrieved distribution.

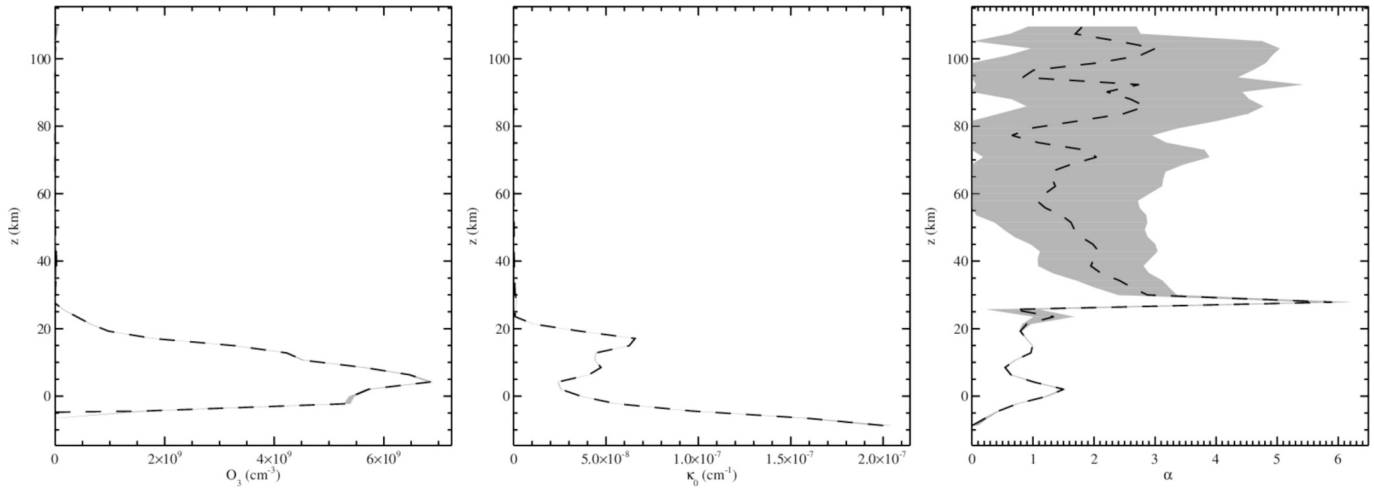

Fig. 12. Results of the inversion of the solar occultation of the Mars atmosphere observed with EXOMARS-NOMAD-UVIS on May 4, 2018, at 0059 UT.. The altitude is estimated from a reference radial distance of 3390 km. Grey shades give the 1-σ standard deviation over the fitting parameters, i.e., from left to right, the ozone density, the differential extinction parameter of the dusts, and the Angström α parameter of the dusts. (Standard UVIS data ID: nmd_cal_sc_uvis_20180504T005927-20,180,504 T011659-e).

dust extinction coefficients can, at least partly, compensate, non-physical negative values being even possibly retrieved by the algorithm, as a consequence of non-linear contamination by noisy variations. It nevertheless remains that, on the very topside, the atmosphere is so tenuous that expecting to retrieve the "true" parameters is somewhat illusory.

4. Preliminary inversion results

The methods developed and presented above can be applied to occultation datasets from spacecraft observing planetary atmospheres known to contain aerosols, such as the atmosphere of Mars. The Trace Gas Orbiter (TGO) of the ExoMars mission of the European Space Agency (ESA) carries the Nadir and Occultation for MArs Discovery (NOMAD) instrument, which comprises three spectrometers, including the UltraViolet/VISible (UVIS) spectrometer, sensitive from 200 to 650 nm [Vandaele et al., 2015]. The NOMAD instrument can be used to remotely sense the vertical profile of the atmosphere recording the absorption of sunlight as it is progressively occulted by the Mars atmosphere along the orbital motion of TGO. The instrument passband includes the ozone Hartley band. Aerosols also produce extinction of the solar UV radiation. It can also be expected that CO_2 can scatter the sun light out of the instrument field of view and produce some extinction. We anticipate over the next paragraphs to warn that preliminary tests conducted on the calibrated NOMAD-UVIS solar occultation data [Mason et al., 2022; Willame et al., 2022] suggest that it appears difficult to retrieve the CO_2 density profile in addition to the ozone and dust profiles, for reasons to be discussed in the next section.

Fig. 12 shows the results of an application of the linear-nonlinear inversion method (Section 3.3) to the ExoMars-NOMAD-UVIS solar occultation of May 4, 2018, at 0059 UT, with a high spectral sampling of ~0.46 nm. Altitude is estimated from a reference radial distance of 3390 km, which can be above the soil of Mars, at places. The inversion was performed over the wavelength range from 240 to 360 nm, the shorter wavelength domain being subject to larger uncertainties owing to the lower solar intensity. A slight smoothing was applied to the UVIS observation to be fitted using the LOWESS method [Clevland, 1985] of first order, with a width of 4.23 km, i.e. corresponding to twice the median altitude bin in the UVIS observation. The retrieved ozone density layer has a profile resembling a Chapman layer with minor disturbances. The dust extinction parameter presents a deep local minimum resulting from two main layers of aerosols. The uncertainties obtained by the inversion process, represented with grey shades, are very small for these parameters and nearly overlap with the lines and appear very dim between the dashes. The α parameter is retrieved with a high accuracy in the altitude range where dusts are abundant (or particularly efficient at extinguishing the UV flux).

Fig. 13 shows the observed and retrieved transmittance corresponding to the vertical profiles of Fig. 12, at four selected wavelengths. The local maximum of the dusts extinction parameter found in the upper part of the profile results in a shoulder observed (and retrieved) at low altitude. The topside shows a weak, progressive attenuation due to the presence of dusts and ozone at low density. At ~250 nm, the solar radiation is attenuated by only ~5 % by the atmosphere above ~20 km. Transmittance oscillations found in that altitude range, especially at shorter wavelengths, do probably not correspond to a real physical phenomenon.

Fig. 14 shows another example of inversion results, obtained for the

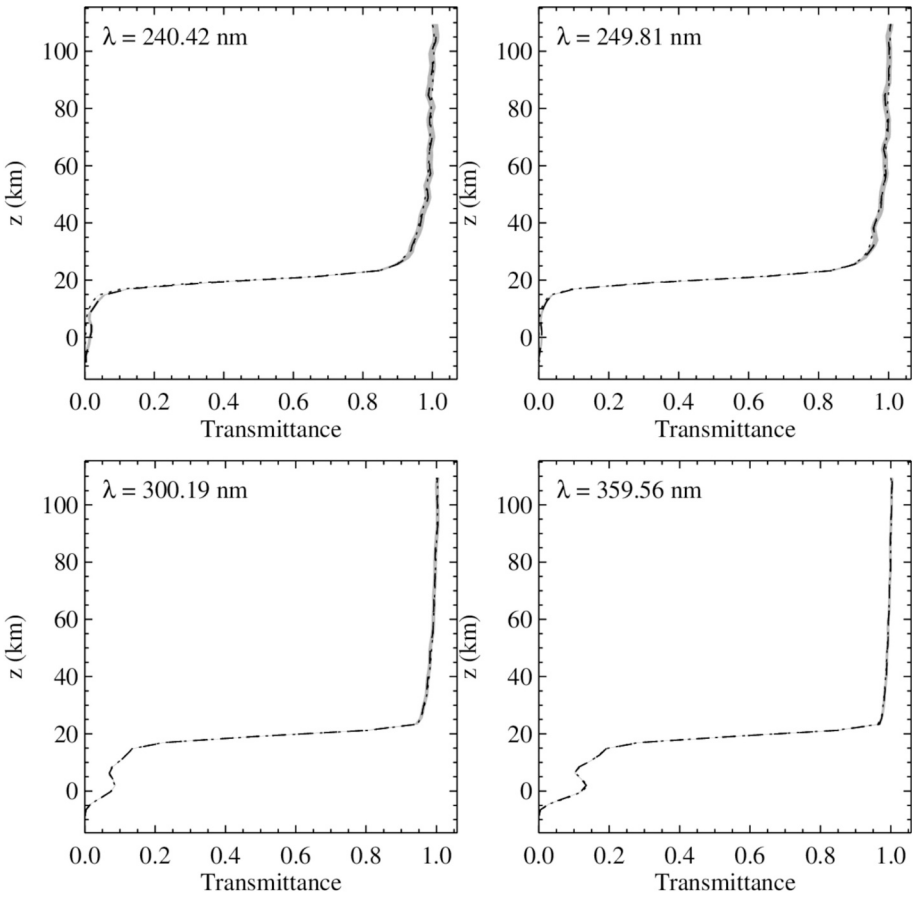

Fig. 13. Observed transmittance (dashed lines) at four different wavelengths using NOMAD-UVIS on May 4, 2018, at 0059 UT. The dashed lines show the transmittance retrieved by the inversion procedure, corresponding to the retrieved atmospheric properties shown in Fig. 12. Observation 1-σ confidence intervals are given by the grey shades. The statistical standard deviation of the retrieved transmittance is very small.

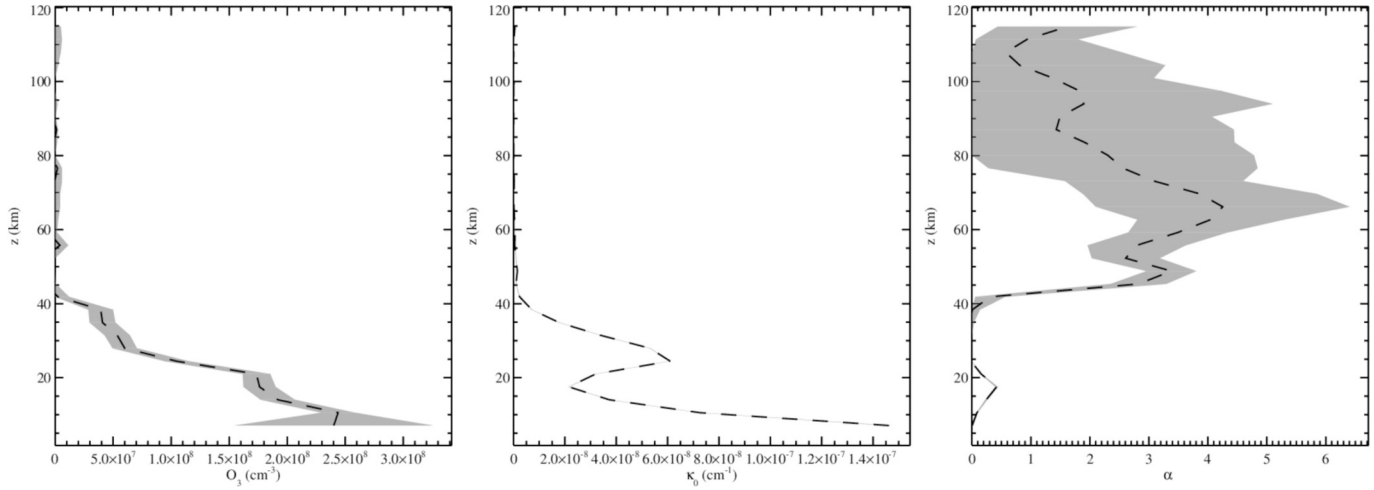

Fig. 14. Same as Fig. 12 for NOMAD-UVIS occultation observation obtained on June 21, 2018, at 0809 UT. (Standard UVIS data ID: nmd_cal_sc_uvis_20180621T080914-20,180,621 T082453-i).

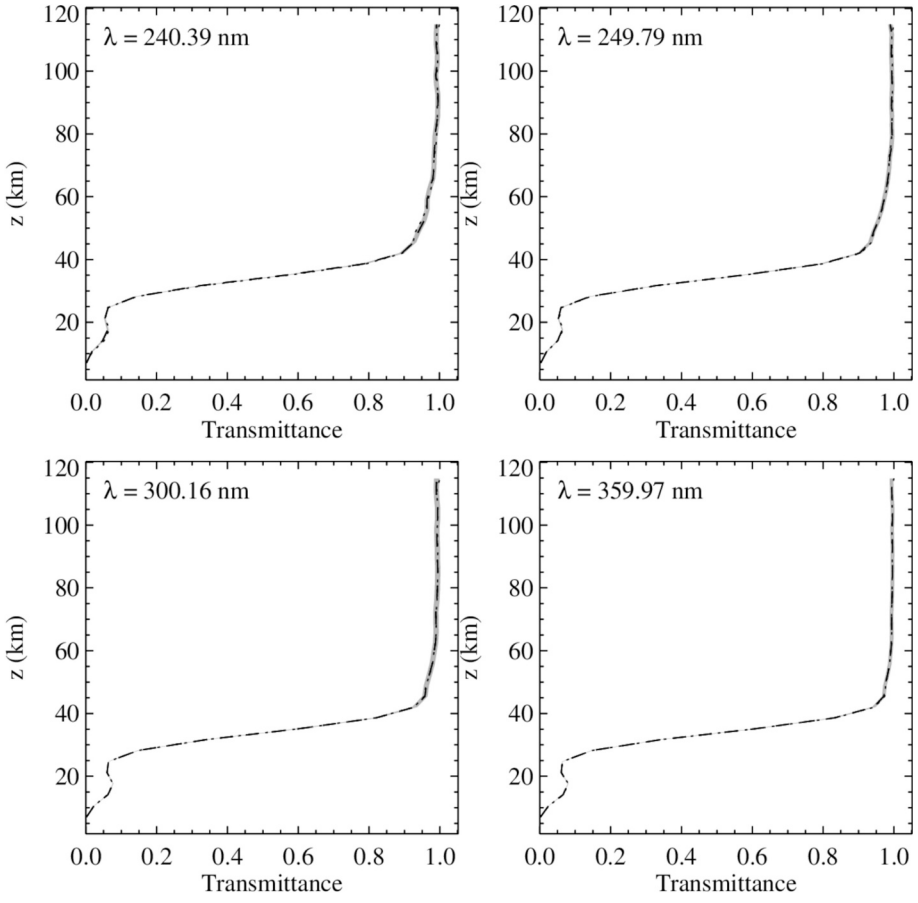

Fig. 15. Same as Fig. 13 for NOMAD-UVIS occultation observation obtained on June 21, 2018, at 0809 UT.

occultation profile recorded on June 21, 2018, at 0809 UT. The retrieved dust extinction parameter profile shows a local maximum above 20 km. As in Fig. 12, the uncertainties over κ_0, represented using grey shades, are very small and appear very dim. The ozone density is an order of magnitude less than the one observed on May 4, 2018, illustrating the high variability of ozone in the atmosphere of Mars. The density being lower, the relative uncertainty is also larger. The detailed fitted transmittance is shown in Fig. 15 at several wavelengths. Agreement between the observations and the fitted values is again very good. Note the local minimum found somewhat above 20 km at all wavelengths: it can be understood as the consequence of the presence of a thin absorbing layer near that altitude range (i.e. somewhat above), consistently with the local maximum found in the aerosol extinction coefficient.

5. Discussion

5.1. Inability of CO_2 retrieval

The first aspect that requires further examination is the inability of the method to reliably retrieve the CO_2 density, although the method conception and testing indicate it should be possible. Indeed, the cross sections used in the tests of the previous paragraphs, as well as in the NOMAD-UVIS inversions above, rather quantify the Rayleigh scattering process. This does not necessarily amount to effective extinction, as it can be speculated that a fraction of the Rayleigh-scattered photons may nevertheless come back to the field of view after further scattering. Quantitatively assessing the importance of that process would, however, require solving completely the radiative transfer of the solar UV radiation through the Mars atmosphere, which is beyond the scope of the present study. It is however expected that this should not produce a very dramatic effect for the following reasons. Resonance scattering is not at play in this problem, so that the optical thickness is not comparable to what would be expected for the oxygen 130.4 nm radiation in the Earth atmosphere, for example. Rayleigh scattering is a less efficient process. For lines of sight nevertheless having a relatively large slant optical thickness, it can be expected that scattered photons will escape the atmosphere upward and seldom reach the instrument because scattering deflects photons at some angle, and photons will travel across larger distances when propagating upward, as it is a direction in which the atmosphere optical thickness is lower owing to the exponential decrease of the gas density with altitude. A photon mean free path therefore represents a longer distance through the atmosphere when it is moving upward. Multiple scattering, when it occurs, therefore has the tendency to funnel the photons upwards, away from the instrument line of sight during occultation observation, especially considering that most of the slant optical thickness is accumulated near the tangent point.

The wavelength dependency of the Rayleigh scattering is a (fourth) power law, functionally similar to that of the aerosols. Consequently, in a real situation, the inversion can turn from an ill-conditioned problem to an ill-posed problem, especially if at some altitude ranges, the aerosols have an Angström parameter close to 4, or if the dusts extinction becomes weak, so that the observation may not allow discriminating between the dusts and CO_2. A misattribution between both therefore becomes possible. One may consider safer ignoring the CO_2 absorption (as was done in the figures of the preceding section), and track cases in which the dusts α parameter is found to be near 4. If, in addition, the dust extinction parameter is found to decrease exponentially with altitude, this would legitimately cast doubts on the physical interpretation of the inversion. A mis-estimation of the wavelength dependency of the extinction cross section also stands among the possible reasons for an inability of an inversion procedure to retrieve that gas concentration.

As extinction is weakly dependent on the CO_2 density in the near UV, the retrieved CO_2 density is, conversely, highly sensitive to small disturbances in the input data used for the inversion as well as to small departures from the underlying hypothesis of the method. Several sources of such disturbances can be considered: any instrument calibration is unavoidably subject to uncertainties. Along the same lines, pre-treatment of the raw data (flat-fielding, background subtraction etc.) is also unavoidably affected by uncertainties as well. Any such uncertainty may slightly affect the input data used in the inversion process, therefore impairing the quality of the retrieved CO_2 without significant consequence over the retrieved O_3 and dust properties, which remain, by design, the main scientific targets of the UVIS instrument in that wavelength range.

Finally, inverse Abel transform relies on a spherical symmetry assumption. By definition, solar occultation observations are obtained near the terminator, i.e. a region where horizontal gradients may easily exist, even moderate ones. A slight breach of the spherical symmetry assumption may well sufficiently disturb the inversion process to prevent a reliable retrieval of the numerically over-sensitive CO_2 density profile. In contrast, as pointed out by Piccialli et al. [2021], horizontal gradients near the terminator are not expected to seriously impair the retrieval of O_3 and of the dust properties. Moreover, our method ignores the weak dependency of the ozone absorption cross section with respect to temperature. This simplifying assumption eliminates an unknown from the problem by assuming a fixed value of the temperature. Strictly speaking, we should use the spectra to estimate the temperature profile as well, and adapt the cross section at all altitude, or rely on an assumed temperature profile. This would anyway lead to an even more complicated retrieval procedure, without warranty that the CO_2 density could be retrieved efficiently, nor that the ozone density would be better estimated given the uncertainties of the inversion method. The breach of both hypotheses nevertheless results in a mathematical description producing an inverse problem that slightly departs from the actual problem we wish to solve. Moreover, the piecewise representation of the physical properties of the atmosphere necessarily departs, even just slightly, from the actual properties of the atmosphere, somewhat disturbing the inversion results as well.

Consequently, given that UV solar occultation is only weakly sensitive to the CO_2 concentration, it is not clear whether it can really be expected retrieving it by analyzing this wavelength range. At the current stage of this preliminary analysis, we could not convincingly establish that CO_2 can reliably be retrieved although, in principle, the inversion software offers the possibility to account for extinction by several gas and to estimate their density in addition to the dust extinction properties. If, in addition, the actual CO_2 density were smaller than the value used in our simulated tests, this weakness inherent to the method and physical properties may appear even more critical.

5.2. Geometry and assumptions

A breach of the spherical symmetry assumption may also arise from other conditions than horizontal gradients along the terminator. The geographic distribution of aerosols may be intrinsically non-symmetric. For example, clouds of icy or solid grains (or of any aerosol) may exist everywhere in a planetary atmosphere, and indeed, water ice clouds have been reported in the literature [e.g. Streeter et al., 2022 and references therein]. The aerosol size and composition may also vary from place to place, leading to asymmetries in the geographic distribution of the Angström parameter. Retrieving the atmosphere properties by inverting remote sensing data obtained from a single vantage point then becomes severely under-constrained by the observation. One would either need observations from several vantage points to be used in a tomographic inversion method, or a smart hypothesis regarding how patchy aerosol populations can exist in the atmosphere and an adapted inversion technique. Unfortunately, none are available at this stage.

The possible existence of very localized layers of aerosols can also complicate the inversion of the observation. If the vertical characteristic scale of such layer (i.e. its thickness and vertical variation scale) is larger than the resolution of both the data and the inversion method, then it can be expected the retrieval method can cope with such a layer. If that scale length is intermediate between the resolution of the observation and of the inversion method, then the retrieval is becoming critical and will likely inaccurately analyze discontinuous variations (as compared to that resolution) in terms of a continuous feature. If the observing resolution becomes poorer than the characteristic scale, then the problem is irremediably impossible to address and the thin, localized layer can hardly be assessed by the observation. As a general matter, the smallest feature size that can be retrieved from observation is limited in a Nyquist sense: we need several observations across a given feature in order to characterize it.

5.3. Numerical aspects

From a theoretical standpoint, we could establish that a globally non-linear fitting method can take advantage of separating the non-linear

and linear fitting parameters and of expressing these latter as functions of the non-linear parameters. The benefit of reducing the number of dimensions of the parameter space can easily outweigh the computational burden of evaluating the derivatives of the linear parameters with respect to the non-linear parameters. Formally, expressing those derivatives remains surprisingly simple, but the software conception is nevertheless more complicated. In this context, including a dynamically weighted regularization in the least squares fit process is also surprisingly easy from a conceptual standpoint, the derivative of the trace of the matrix of the system requiring regularization remaining easy to compute without incurring a heavy computational cost.

Estimating uncertainties over the fitting parameters is often a delicate task. We evaluate the uncertainties applying the usual methods used in pseudo-Newton fitting algorithms, which use a computationally cheap approximation of the Hessian matrix based on first derivatives only. Those estimates generally assume that the uncertainties of the data follow a Gaussian statistical distribution. In the case of the inversion of occultation observations, the logarithm of the transmittance is the input of the fitting procedure, and the uncertainties of this logarithm are not expected to remain Gaussian. We conducted a bootstrapping test that indicates that the uncertainties over the fitting parameters remain correctly estimated despite the breakdown of the Gaussian hypothesis used in pseudo-Newton methods.

An analysis of the exact Hessian matrix of the least squares fit method was conducted near the fitting solution found by the applied Levenberg-Marquardt method. Near convergence, this algorithm becomes equivalent to a pseudo-Newton method. It was found that, despite the eigenvalues of the pseudo-Hessian matrix are all positive, a few of those of the exact Hessian matrix can be slightly negative. This indicates the algorithm mis-identified a saddle point as a local minimum. This is however less dramatic than it may seem. It is clear that the whole transmittance vertical profile is only weakly sensitive to the topside atmospheric properties, where the gas and dust densities are very low. The chi-square function is therefore weakly sensitive to the topside fitting parameters, compared with those determined at altitudes where the bulk of the attenuation takes place, so that only unimportant parameters have a fitted value that may depart from the actual one. Indeed, our simulated tests indicate that the top-side parameters are not necessarily perfectly retrieved. This can be due to a border effect as well as to this misidentification issue. Conversely, it can hardly be expected determining the value of parameters over which the observation is nearly not sensitive, producing therefore a χ^2 function looking like a deep, flat (multidimensional) valley along the directions of variations of those parameters. As a general matter, we nevertheless warn that pseudo-Newton methods enforce a zero gradient condition, but do not guarantee for sure that a local minimum will be found, although in general, the pseudo-Hessian approximation suffices to reach a true minimum. Several ideas can be considered to mitigate the problem. We suggest that, in the case of inverse Abel transform methods, adding to the pseudo-Hessian matrix a few contributions of the second derivative terms at and near the diagonal could perhaps help mitigating the problem at a relatively moderate computational cost. This would however require an in-depth re-thinking of the Levenberg-Marquardt algorithm and of pseudo-Newton methods in general. Adopting a totally different fitting method could also be considered. Possible candidates are the Nelder-Mead down-hill simplex (including simulated annealing or not) [Press et al., 1992], or swarm minimization techniques [see, e.g. Fajr and Bouroumi, 2020; Banks et al., 2007; 2008]. It is however expected that those methods will have a prohibitively high computational cost to offer a workable mean to treat a large, extensive satellite dataset, at least using currently available microprocessors. Indeed, we tested the Nelder-Mead algorithm and found that reaching convergence can take a long time, and that it requires being initialized with a very good first guess without necessarily giving a result more reliable than the Levenberg-Marquardt method. An elementary implementation of a swarm minimization was attempted, but it convinced us that the computational cost will remain prohibitive in a foreseeable future.

5.4. Application to NOMAD-UVIS observations

Application of the linear-nonlinear method to real NOMAD-UVIS observations indicates that the method produces reasonable estimates of the O_3 density profile and dusts properties. We notice that, because the solar flux at shorter UV wavelengths is relatively low, it can suffice restricting the wavelength range in the low wavelength domain. Extending somewhat the range to longer wavelengths is feasible and helps obtaining reasonable ozone density profiles and dust properties, but does not suffice to recover the CO_2 profile. As expected, the dust extinction parameter profiles can be retrieved even when it presents local extrema. Recovering the CO_2 density can certainly be achieved including additional data collected in another wavelength domain, as proposed by [Trompet et al., 2023a, 2023b], using infrared observations near 3 μm. CO_2 absorption at shorter wavelength, in the FUV domain, may also be considered, given that the CO_2 absorption cross section reaches a local maximum near 130 nm, as shown by Yoshino et al. [1996] and Parkinson et al. [2003]. This wavelength range may, however, present the difficulty of excluding the effect of the resonance scattering of the $O(^3P)$ triplet at 130.4 nm and of the carbon multiplets at 126.1, 156.1 and 165.7 nm. Knowing the CO_2 density profile may also allow us to include the temperature dependency of the ozone absorption cross section. It is however not expected that this further refinement would dramatically modify the results, given the temperature range to be accounted for and the unavoidable uncertainties of inversion methods. A reasonable temperature dependency could nevertheless be included in two manners. First, one may use a model output, providing a realistic temperature profile, though not necessarily the exact one. Second, one may obtain it from the slope of the CO_2 density profile as was done by Trompet et al. [Trompet et al., 2023a, 2023b]. This profile may be limited in altitude when spectral saturation occurs at large optical depth [Trompet et al., 2023b], which may require combining the observation-derived temperature with model outputs.

Adapting the regularization level (with parameter c in Eq. (42)) could be considered critical. Trompet et al. [Trompet et al., 2023a] examined several strategies to adapt regularization, which they apply to another inversion method. They found that a total error minimization technique [Xu et al., 2016] appears the most efficient technique to be used in their inversion technique. Morozov's discrepancy principle may also be considered [Morozov, 1966; Vogel, 2002]. Regularization methods generally rely on eigenvalues filtering, such as the Tickhonov-Philips method, with regularization level selection that either depends on some knowledge of the problem solution and noise characteristics, or on so-called a posteriori estimate such as the Morozov principle [Vogel, 2002]. Those methods are generally particularly suited for linear problems, and may require several inversion attempts to pick a suitable regularization level. Our method includes non-linear parameters, i.e. the α parameters, and all other parameters are expressed as functions of the α, including the regularization weighting through the trace of the linear system that needs to be solved for each function evaluation. In a sense, the simple method we choose still accounts for the problem characteristics by comparing the trace of the χ^2-derived matrix and the regularization matrix. The main goal here is not so much to smooth the retrieved quantities than to protect the whole fitting procedure from nearly singular matrix inversion, which would both amplify the effects of noise and prevent proper parameters retrieval. So the trace ratio weighting is lowered by a multiplication by a small c parameter. We tested that keeping this c parameter below $\sim 10^{-2}$–10^{-3} suffices, without too much altering the retrieved parameters. The choice made here is particularly suited to our method, since it allows to smoothly adapt the regularization level to the α-dependent fitting matrix, the derivative of the trace ratio being surprisingly easy to evaluate at a moderate computational cost. Estimating the regularization weight according to other principles would make the derivative computation intractable. Further

improvements may however be considered, for example, by analyzing the eigenvalues of the χ^2 minimization system at the end of the fitting problem and restart the non-linear fitting procedure using a c value updated according to a comparison between the largest and smallest eigenvalues. It is however not expected this would produce a dramatic modification of the retrieved results as c is already small and no singular system has been encountered when the method was applied to a number of observed profiles.

We also mention here that additional preliminary analysis has been performed on NOMAD-UVIS data having a somewhat lower wavelength resolution. In that case, the wavelength resolution of the extinction cross section of ozone is degraded and reduced, averaging the value of the high resolution cross section over each low resolution bin with a weighting by the solar spectrum. Under a spectral resolution of 1.9 nm, the retrieved dust properties and ozone density profiles then present reasonable characteristics, compatible with what is expected in the Martian atmosphere. This does however not guarantee that the retrieved parameters are insensitive to the spectral resolution of the observation.

5.5. Spurious ozone detection

Retrieval of trace gases from occultation observations has the recurrent weakness of being exposed to so-called spurious identifications, as was extensively discussed by Määttänen et al. [2022] and Piccialli et al. [2023], who identified erroneous estimate of ozone density inherently due to the observation technique. They propose several filtering methods to cope with this issue and exclude spurious ozone detections. Our method is no exception to this problem and we identified several cases of spurious ozone detection. It is anticipated that systematic analysis of a broad database will require the development of misestimate identification techniques as well, which may be specific of the method and used wavelength range. The reason behind spurious ozone detection is thought to stem from the sometimes very low ozone density of planet Mars. In that case, the least squares fitting algorithm uses the degrees of freedom allowed by the fitting parameters aimed at the ozone retrieval to overfit the data instead of just giving zero concentrations. In a sense, the problem then becomes ill-posed instead of being ill-conditioned. From a photochemical perspective, previous studies based on inversion techniques have indicated a relation between ozone and water vapor, which reacts with O_3 [Patel et al., 2021; Khayat et al., 2021]. When the water vapor is more abundant in the atmosphere, the ozone destruction rate is enhanced, which can drastically reduce the ozone abundance. Moreover, water vapor and dusts have been found to be interdependent [Streeter et al., 2022], so that it appears valuable studying the aerosol, ozone and water profiles simultaneously, highlighting a complex photochemistry possibly dependent on retroactions and feedbacks.

6. Conclusions

Three different methods have been introduced from a theoretical and numerical standpoint to evaluate the inverse Abel transform of occultation observations of a planetary atmosphere containing several absorbing gas and aerosols, such as the Mars atmosphere. All methods rely on a piecewise analytic representation of the altitude-dependent parameters to be retrieved and their direct Abel transform along observation line-of-sights, least-squares fitting of those parameters to match the observed wavelength-dependent extinction scan obtained at a set of tangent altitudes, and regularization techniques applied to cope with the possible ill-conditioning of the inverse problem. Inclusion of aerosol extinction assumes a power dependency with respect to wavelength, while extinction by atmospheric gas is computed using known extinction cross sections.

The first method proceeds in two steps: wavelength-by-wavelength least-squares based inversion of the observed transmittance and total optical thickness of the atmosphere followed by least squares determination of the fitting parameters at each fitting altitude. It is tested that this method allows the retrieval of the atmosphere properties at little computational cost, even when a realistic noise is included in the tests. It is however argued that the two-steps procedure does not necessarily account for the possible covariance between the fitted parameters, especially under noise contamination, and that, in principle, it is preferable determining all the fitting parameters at once in a single leas-squares fitting procedure. The main advantage of the method remains its small computational cost as the non-linearity of the fitting problem only appears in the second fitting step, where only one non-linear parameter appears.

The second method uses a Levenberg-Marquardt fitting algorithm assuming all the parameters leading to a linear variation of the optical thickness can be expressed as functions of the parameters with respect to which the extinction optical thickness varies non-linearly. The linear parameters are the gas local concentrations and the aerosols local extinction coefficients at a reference wavelength of interest, while the non-linear parameters are the local power coefficients governing the wavelength dependance of the aerosols extinction, i.e. the so-called Angström or α parameter. The gas concentration and dust extinction parameter at reference wavelength are represented as piecewise linear functions of the radial distance, while the non-linear α parameter profile is represented using a piecewise linear function of the logarithm of the radial distance, which can be used advantageously in numerical evaluation of the line-of-sight integrated optical thickness of the dusts, and even reduce to analytic expressions using hypergeometric ${}_2F_1$ functions. It is found that this method reduces the computational cost of the fitting by reducing the number of dimensions of the parameter space spanned by the fitting algorithm in its search for an optimum. It also allows for an estimate of the uncertainties affecting all the relevant physical parameters, without risk of misaccounting for covariances since all parameters are determined at once using all the observations simultaneously. Our tests indicate that this combined linear-nonlinear method can retrieve the needed fitting parameters (including the linear parameters) even when a noise contamination is accounted for. We also verified using a boot strapping test that the error retrieved by our method matches the dispersion of the results of the boot strap sampling. We note that the Levenberg-Marquardt algorithm evolves into a pseudo-Newton method near the determined optimum, which uses a pseudo-Hessian matrix, so that the algorithm can stop at a saddle point when the inversion problem is very weakly dependent on some of its parameters. Those less relevant parameters may then be poorly retrieved by any inversion algorithm.

The third method presented here uses a piecewise exponential approximation for the gas species, and uses a fully non-linear fitting method to perform the inversion. It is found that this method is computationally very expensive, with only marginal improvement compared with the second method. We note that this method requires initialization at a very good first guess to have the fitting algorithm reach convergence.

Preliminary tests have been conducted on observations from the NOMAD-UVIS solar occultation UV channel. It is found that the aerosol properties and O_3 density profiles can be retrieved using the second, linear-nonlinear method, with a very good accuracy. However, in this wavelength range, extinction depends too weakly on the CO_2 density profile to allow reliably retrieving it.

CRediT authorship contribution statement

B. Hubert: Writing – original draft, Visualization, Validation, Supervision, Software, Methodology, Investigation, Formal analysis, Conceptualization. **L. Soret:** Writing – original draft, Resources, Conceptualization. **J.-C. Gérard:** Writing – original draft, Supervision, Conceptualization. **G. Wautelet:** Writing – original draft, Conceptualization. **G. Munhoven:** Methodology, Formal analysis, Conceptualization. **A. Piccialli:** Methodology, Conceptualization. **A.-C. Vandaele:** Supervision, Resources.

Declaration of competing interest

The authors declare that they have no known competing financial interests or personal relationships that could have appeared to influence the work reported in this paper.

Data availability

Data will be made available on request.

Acknowledgments

B. Hubert and G. Munhoven are Research Associates of the Fonds de la Recherche Scientifique – FNRS. The authors thank M. W. Buie, Lowell Observatory, for making his lowess filter subroutine publicly available. The NOMAD experiment is led by the Royal Belgian Institute for Space Aeronomy (IASB-BIRA), assisted by Co-PI teams, from Spain (IAA-CSIC), Italy (INAF-IAPS), and the United Kingdom (Open University). This project acknowledges funding by the Belgian Science Policy Office (BELSPO), with the financial and contractual coordination by the ESA Prodex Office (PEA4000103401, 4000121493), by Spanish Ministry of Science and Innovation (MCIU) and by European funds under grants PGC2018-101836-B-I00 and ESP2017-87143-R (MINECO/FEDER), as well as by UK Space Agency through grants ST/V002295/1, ST/V005332/1 and ST/S00145X/1 and Italian Space Agency through grant 2018-2-HH.0. This work was supported by the Belgian Fonds de la Recherche Scientifique – FNRS under grant number 30442502 (ET_HOME). The IAA/CSIC team acknowledges financial support from the State Agency for Research of the Spanish MCIU through the 'Center of Excellence Severo Ochoa' award for the Instituto de Astrofísica de Andalucía (SEV-2017-0709). G. Wautelet is supported by the BELSPO – IREC2020 project. Lauriane Soret is supported by the FNRS and the University of Liège.

References

Abramowitz, M., Stegun, I., 1972. Handbook of Mathematical Functions with Formulas, Graphs and Mathematical Tables. Dover Publications, New York.

Amiri, H.E.S., et al., 2022. The Emirates Mars mission. Space Sci. Rev. 218, 1. https://doi.org/10.1007/s11214-021-00868-x.

Angström, A., 1929. On the atmospheric transmission of sun radiation and on dust in the air. Geograf. Ann. Deut. 11, 156–166.

Banks, A., Vincent, J., Anyakoha, C., 2007. A review of particle swarm optimization. Part I: background and development. Nat. Comput. 6, 467–484.

Banks, A., Vincent, J., Anyakoha, C., 2008. A review of particle swarm optimization. Part II: hybridisation, combinatorial, multicriteria and constrained optimization, and indicative applications. Nat. Comput. 7, 109–124.

Bracewell, R., 1999. The Fourier Transform and its Applications, 3 ed. McGraw-Hill, New York.

Clevland, W.S., 1985. The Elements of Graphing Data, Wadsworth Advanced Books and Software. ISBN: 0534037291, 9780534037291.

Colin, L., Hall, C.F., 1977. The Pioneer Venus program. Space Sci. Rev. 20, 283–306.

Colin, L., Hunten, D.M., 1977. Pioneer Venus experiment description. Space Sci. Rev. 20, 451–525.

Fajr, R., Bouroumi, A., 2020. An improved particle swarm optimization algorithm for global multidimensional optimization. J. Intell. Syst. 29 (1), 127–142. https://doi.org/10.1515/jisys-2017-0104.

Forget, F., Montmessin, F., Bertaux, J.L., González-Galindo, F., Lebonnois, S., Quémerais, E., et al., 2009. Density and temperatures of the upper Martian atmosphere measured by stellar occultations with Mars Express SPICAM. J. Geophys. Res. 114 (1), 1004. https://doi.org/10.1029/2008JE003086.

Gupta, S., Yelle, R.V., Schneider, N.M., Jain, S.K., Gonzalez-Galindo, F., Verdier, L., et al., 2022. Thermal structure of the Martian upper mesosphere/lower thermosphere from MAVEN/IUVS stellar occultations. J.Geophys. Res. 127, e2022JE007534. https://doi.org/10.1029/2022JE007534.

Hartley, W.N., 1881. On the absorption spectrum of ozone. J. Chem. Soc. Trans. 39, 111. https://doi.org/10.1039/CT8813900111.

Hubert, B., Opitom, C., Hutsemekers, D., Jehin, E., Munhoven, G., Manfroid, J., Bisikalo, D.V., Shematovich, V.I., 2016. An inversion method for cometary atmospheres. Icarus. https://doi.org/10.1016/j.icarus.2016.04.044.

Hubert, B., Opitom, C., Hutsemekers, D., Jehin, E., Munhoven, G., Manfroid, J., Bisikalo, D.V., Shematovich, V.I., 2022. Analytic and numerical methods for the abel transform of exponential functions for planetary and cometary atmospheres. Icarus. https://doi.org/10.1016/j.icarus.2021.114654.

Jakosky, B.M., et al., 2015. The mars atmosphere and volatile evolution (MAVEN) mission. Space Sci. Rev. 195 (1–4), 3–48. ISSN 15729672. https://doi.org/10.1007/s11214-015-0139-x.

Khayat, A.S.J., et al., 2021. ExoMars TGO/NOMAD-UVIS vertical profiles of ozone: 2. The high-altitude layers of atmospheric ozone. J. Geophys. Res. 126, e2021JE006834. https://doi.org/10.1029/2021JE006834.

Krasnopolski, V.A., 2002. Mars' upper atmosphere and ionosphere at low, medium, and high solar activities: implications for evolution of water. J. Geophys. Res. 107. https://doi.org/10.1029/2001JE001809.

Kumar, A.S.K., Chauhan, P., 2014. Scientific exploration of Mars by first Indian interplanetary space probe: Mars orbiter mission. Curr. Sci. 107, 1096.

Lebonnois, S., Quémerais, E., Montmessin, F., Lefèvre, F., Perrier, S., Bertaux, J.-L., Forget, F., 2006. Vertical distribution of ozone on mars as measured by SPICAM/mars express using stellar occultations. J. Geophys. Res. 111.

Määttänen, A., Litowski, C., Montmessin, F., Maltagliati, L., Reberac, A., Joly, L., Bertaux, J.-L., 2013. A complete climatology of the aerosol vertical distribution on Mars from Mex/SPICAM UV solar occultations. Icarus 223, 892. https://doi.org/10.1016/j.icarus.2012.12.001.

Määttänen, A., Lefèvre, F., Verdier, L., Montmessin, F., Listowski, C., Guilbon, S., Fedorova, A., Korablev, O., 2022. Ozone vertical distribution in Mars years 27–30 from SPICAM/MEX UV occultations. Icarus 387, 115162. https://doi.org/10.1016/j.icarus.2022.115162.

Malicet, J., Daumont, D., Charbonnier, J., Parisse, C., Chakir, A., Brion, J., 1995. Ozone UV spectroscopy. II. Absorption cross-sections and temperature dependence. J. Atmos. Chem. 21, 263–273. https://doi.org/10.1007/BF00696758.

Mason, J.P., et al., 2022. Removal of straylight from ExoMars NOMAD-UVIS observations. Planet. Space Sci. 218, 105432.

Montmessin, F., Quémerais, E., Bertaux, J.L., Korablev, O., Rannou, P., Lebonnois, S., 2006. Stellar occultations at UV wavelengths by the SPICAM instrument: retrieval and analysis of Martian haze profiles. J. Geophys. Res. 111, E09S09. https://doi.org/10.1029/2005JE002662.

Morozov, V., 1966. On the solution of functional equations by the method of regularization. Dokl. Akad. Nauk SSSR 167 (3), 510–512.

Neefs, E., Vandaele, A.C., Drummond, R., Thomas, I.R., Berkenbosch, S., Clairquin, R., et al., 2015. NOMAD spectrometer on the ExoMars trace gas orbiter mission: part 1—design, manufacturing and testing of the infrared channels. Appl. Opt. 54 (28), 8494. https://doi.org/10.1364/ao.54.008494.

Olver, F.W., Lozier, D.W., Boisvert, R.F., Clark, C.W., 2010. NIST Handbook of Mathematical Functions, 1st ed. Cambridge University Press, New York, NY, USA.

O'Neill, N., Royer, A., 1993. Extraction of bimodal aerosol-size distribution radii from spectral and angular slope (Angström) coefficients. Appl. Opt. 32, 1642.

Parkinson, W.H., Rufus, J., Yoshino, K., 2003. Absolute absorption cross section measurements of CO_2 in the wavelength region 163–200 nm and the temperature dependence. Chem. Phys. 290, 251–256. https://doi.org/10.1016/S0301-0104(03)00146-0.

Patel, M., et al., 2017. NOMAD spectrometer on the ExoMars trace gas orbiter mission: part 2-design, manufacturing, and testing of the ultraviolet and visible channel. Appl. Opt. 56 (10), 2771. https://doi.org/10.1364/AO.56.002771.

Patel, M., et al., 2021. ExoMars TGO/NOMAD-UVIS vertical profiles of ozone: 1. Seasonal variation and comparison to water. J. Geophys. Res. 126, e2021JE006837. https://doi.org/10.1029/2021JE006837.

Piccialli, A., Vandaele, A.C., Trompet, L., Neary, L., Viscardy, S., Erwin, J.T., Määttänen, A., Daerden, F., Willame, Y., Robert, S., Aoki, S., Wilquet, V., Lefèvre, F., Montmessin, F., 2021. Impact of gradients at the martian terminator on the retrieval of ozone from SPICAM/Mex. Icarus 353, 113598. https://doi.org/10.1016/j.icarus.2019.113598.

Piccialli, A., Vandaele, A.C., Willame, Y., Määttänen, A., Trompet, L., Erwin, J.T., et al., 2023. Martian ozone observed by TGO/NOMAD-UVIS solar occultation: an inter-comparison of three retrieval methods. Earth Space Sci. 10, e2022EA002429.

Press, W.H., Flannery, B.P., Teukolsky, S.A., Vetterling, W.T., 1992. Numerical Recipes in Fortran 77. The Art of Scientific Computing, 2 ed. Cambrige University Press, Cambridge.

Quémerais, E., Bertaux, J.L., Korablev, O., Dimarellis, E., Cot, C., Sandel, B.R., Fussen, D., 2006. Stellar occultations observed by SPICAM on Mars express. J. Geophys. Res. 111 (9), 9–13. https://doi.org/10.1029/2005JE002604.

Streeter, P.M., Sellers, G., Wolff, M.J., Mason, J.P., Patel, M.R., Lewis, S.R., et al., 2022. Vertical aerosol distribution and mesospheric clouds from ExoMars UVIS. J. Geophys. Res. 127, e2021JE007065. https://doi.org/10.1029/2021JE007065.

Svedhem, H., et al., 2007. Venus express—the first European mission to Venus. Planet. Space Sci. 55, 1636–1656. https://doi.org/10.1016/j.pss.2007.01.013.

Tobiska, W.K., Woods, T., Eparvier, F., Vierek, R., Floyd, L., Bouwer, D., Rotman, G., White, O.R., 2000. The SOLAR2000 empirical SOLAR irradiance model and forecast tool. J. Atmos. Sol. Terr. Phys. 62, 1233. https://doi.org/10.1016/j.icarus.2023.115839.

Trompet, L., et al., 2023a. Carbon dioxide retrievals from NOMAD-SO on ESA's ExoMars trace gas orbiter and temperature profiles retrievals with the hydrostatic equilibrium equation: 1. Description of the method. J. Geophys. Res. 128, e2022JE007277. https://doi.org/10.1029/2022JE007277.

Trompet, L., et al., 2023b. Carbon dioxide retrievals from NOMAD-SO on ESA's ExoMars trace gas orbiter and temperature profile retrievals with the hydrostatic equilibrium equation: 2. Temperature variabilities in the mesosphere at Mars terminator. J. Geophys. Res. 128, e2022JE007279. https://doi.org/10.1029/2022JE007279.

Vago, J., Witasse, O., Svedhem, H., Baglioni, P., Haldemann, A., Gianfiglio, G., Blancquaert, T., McCoy, D., de Groot, R., 2015. ESA ExoMars program: the next step in exploring Mars. Solar System Research 49 (7), 518–528. https://doi.org/10.1134/S0038094615070199.

Vandaele, A.C., Neefs, E., Drummond, R., Thomas, I.R.R., Daerden, F., Lopez-Moreno, J.-J.J., et al., 2015. Science objectives and performances of NOMAD, a spectrometer suite for the ExoMars TGO mission. Planet. Space Sci. 119, 233–249. https://doi.org/10.1016/j.pss.2015.10.003.

Vogel, C.R., 2002. Computational Methods for Inverse Problems. SIAM, Philadelphia, USA. ISBN 0–89871–507-5.

Willame, Y., et al., 2022. Calibration of the NOMAD-UVIS data. Planet. Space Sci. 218, 105514. https://doi.org/10.1016/j.pss.2022.105504.

Xu, J., Schreier, F., Doicu, A., Trautmann, T., 2016. Assessment of Tikhonov-type regularization methods for solving atmospheric inverse problems. JQSRT 184, 274–286. https://doi.org/10.1016/j.jqsrt.2016.08.003.

Yoshino, K., Esmond, J.R., Sun, Y., Parkinson, W.H., Ito, K., Matsui, T., 1996. Absorption cross section measurements of carbon dioxide in the wavelength region 118.7-l75.5 nm and the temperature dependence. J. Quant. Spectrosc. Radiat. Transf. 55, 1, 53–60. https://doi.org/10.1016/0022-4073(95)00135-2.